The chaperone DNAJB6 surveils FG-nucleoporins and is required for interphase nuclear pore complex biogenesis

Kuiper, E. F. Elsiena; Gallardo, Paola; Bergsma, Tessa; Mari, Muriel; Kolbe Musskopf, Maiara; Kuipers, Jeroen; Giepmans, Ben N.G.; Steen, Anton; Kampinga, Harm H.; Veenhoff, Liesbeth M.

Published in:
Nature Cell Biology

DOI:
10.1038/s41556-022-01010-x

Publication date:
2022

nature cell biology

Letter

https://doi.org/10.1038/s41556-022-01010-x

The chaperone DNAJB6 surveils FG-nucleoporins and is required for interphase nuclear pore complex biogenesis

Received: 26 October 2021

Accepted: 12 September 2022

Published online: 27 October 2022

Check for updates

E. F. Elsiena Kuiper[1,4] ✉, Paola Gallardo[2,7], Tessa Bergsma[2,7], Muriel Mari[1,5,7], Maiara Kolbe Musskopf[1], Jeroen Kuipers[1,3], Ben N. G. Giepmans[1], Anton Steen[2], Harm H. Kampinga[1] ✉, Liesbeth M. Veenhoff[2] ✉ and Steven Bergink[1,6] ✉

Biogenesis of nuclear pore complexes (NPCs) includes the formation of the permeability barrier composed of phenylalanine-glycine-rich nucleoporins (FG-Nups) that regulate the selective passage of biomolecules across the nuclear envelope. The FG-Nups are intrinsically disordered and prone to liquid–liquid phase separation and aggregation when isolated. How FG-Nups are protected from making inappropriate interactions during NPC biogenesis is not fully understood. Here we find that DNAJB6, a molecular chaperone of the heat shock protein network, forms foci in close proximity to NPCs. The number of these foci decreases upon removal of proteins involved in the early steps of interphase NPC biogenesis. Conversely, when this process is stalled in the last steps, the number of DNAJB6-containing foci increases and these foci are identified as herniations at the nuclear envelope. Immunoelectron tomography shows that DNAJB6 localizes inside the lumen of the herniations arising at NPC biogenesis intermediates. Loss of DNAJB6 results in the accumulation of cytosolic annulate lamellae, which are structures containing partly assembled NPCs, a feature associated with disturbances in NPC biogenesis. We find that DNAJB6 binds to FG-Nups and can prevent the aggregation of the FG region of several FG-Nups in cells and in vitro. Together, our data show that the molecular chaperone DNAJB6 provides quality control during NPC biogenesis and is involved in the surveillance of native intrinsically disordered FG-Nups.

Nuclear pore complexes (NPCs) are the sole gateways between the nucleus and the cytoplasm of the eukaryotic cell and consist of an eight-fold symmetrical cylindrical structure embedded in the double membrane of the nuclear envelope (NE). Being one of the largest protein complexes in cells, the NPC consists of over 30 different proteins, the nucleoporins (Nups), each present in multiple copies (reviewed in refs. [1–4]). Assembling such a large multi-subunit structure while fusing the membranes of the NE, plus the propensity of the FG-Nups to

[1]Department of Biomedical Sciences of Cell & Systems, University of Groningen, University Medical Center Groningen, Groningen, the Netherlands. [2]European Research Institute for the Biology of Ageing, University of Groningen, University Medical Center Groningen, Groningen, the Netherlands. [3]UMCG Microscopy and Imaging Center (UMIC), University of Groningen, University Medical Center Groningen, Groningen, the Netherlands. [4]Present address: Department of Molecular Biophysics and Biochemistry, Yale University, New Haven, CT, USA. [5]Present address: Department of Biomedicine, Aarhus University, Aarhus, Denmark. [6]Present address: University College, University of Groningen, Groningen, the Netherlands. [7]These authors contributed equally: Paola Gallardo, Tessa Bergsma, Muriel Mari. ✉e-mail: elskuiper@gmail.com; h.h.kampinga@umcg.nl; l.m.veenhoff@rug.nl; s.bergink@rug.nl

https://doi.org/10.1038/s41556-022-01010-x

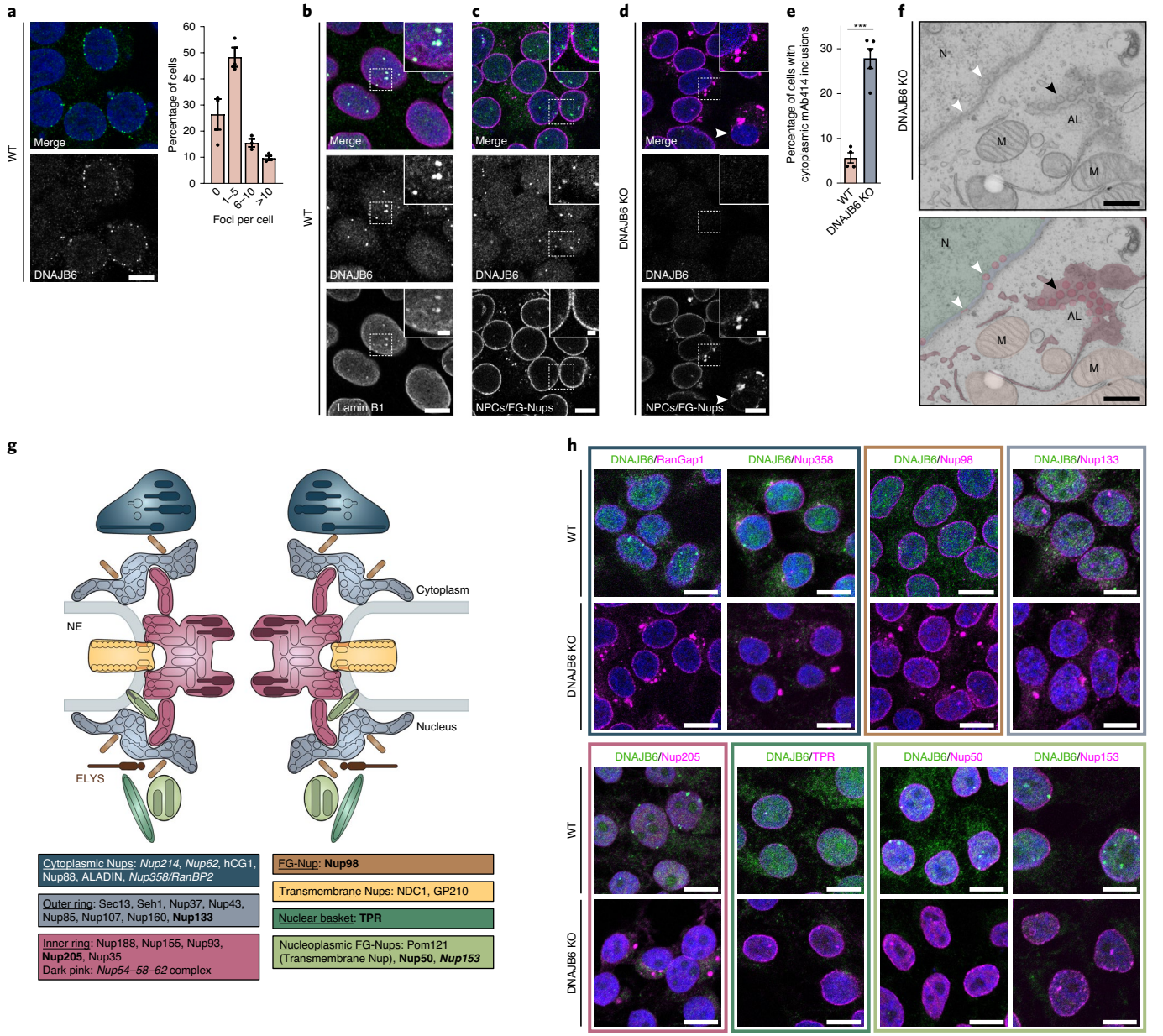

Fig. 1 | DNAJB6 localizes in foci to the NE, and disruption of DNAJB6 expression leads to accumulation of annulate lamellae. a, HEK293T cells stained for DNAJB6 show foci at the NE (Supplementary Video 1 for *Z*-stack, and Extended Data Fig. 1a for a *Z*-projection). Graph depicts a quantification of the distribution of the number of DNAJB6 foci per cell. $n = 3$ independent experiments with 1,272 cells examined; mean ± s.e.m. Over 75% of cells have one or more foci at the NE at a given time. **b**, HEK293T cells stained for DNAJB6 (green) and Lamin B1 (magenta) show co-localization of Lamin B1 with DNAJB6 foci (focused near the top of the nucleus). **c**, HEK293T WT cells stained for DNAJB6 (green) and NPCs/FG-Nups with mAb414 (magenta). **d**, HEK293T DNAJB6 KO cells stained for DNAJB6 (green) and NPCs (mAb414, magenta) have distinct cytoplasmic accumulations of NPCs. Arrows indicate areas of the NE where NPCs are more irregularly distributed. **e**, Quantification of percentage of cells with cytoplasmic NPC accumulations. $n = 4$ independent experiments for WT and $n = 5$ independent experiments for DNAJB6 KO; unpaired *t*-test, two-tailed *P* value; ***$P < 0.0001$; mean ± s.e.m. **f**, Cytoplasmic NPC accumulations (annulate lamellae) visualized by TEM. NPCs, pseudo-coloured in bright pink, can be distinguished in the NE and in cytoplasmic sheets. Black arrowheads point at individually identifiable NPCs in annulate lamellae and white arrowheads at NPCs in the NE. Nucleus (green) indicated with N, NE light blue, mitochondria (light pink) indicated with M, and ER dark pink. Scale bar represents 500 nm. **g**, Schematic overview of the NPC, adapted from Fernandez-Martinez & Rout[1]. FG-Nups in the central channel are dark pink. Indicated in italic are NPC components stained by the mAb414 antibody. Indicated in bold are NPC components stained for in **h**. **h**, RanGap1, and the different Nups of the NPC, that is, Nup358, Nup133, Nup205, Nup98, TPR, Nup50 and Nup153, are stained (magenta) together with DNAJB6 (green) in WT and DNAJB6 KO cells (for individual channels, see Extended Data Fig. 1i). Scale bars on all fluorescent images represent 10 µm, and on magnifications 2 µm. Source numerical data are available in source data.

liquid–liquid phase separate[5,6] and aggregate[7], make NPC biogenesis a multi-step and complex event. Appearance of misassembled NPC intermediates or damaged NPCs is a risk to the cell as it could possibly lead to loss of compartmentalization. In ageing, as well as in disease, it becomes clear how NPC function is intricately interwoven with cell physiology, as in both instances a loss of NPC function has been observed[8–11]. In particular, dividing cells depend on a constant supply of new NPCs, and indeed NPC assembly is compromised in mitotically aged yeast cells[10].

The mechanisms how FG-Nups are protected from making inappropriate interactions during NPC biogenesis are only beginning to

https://doi.org/10.1038/s41556-022-01010-x

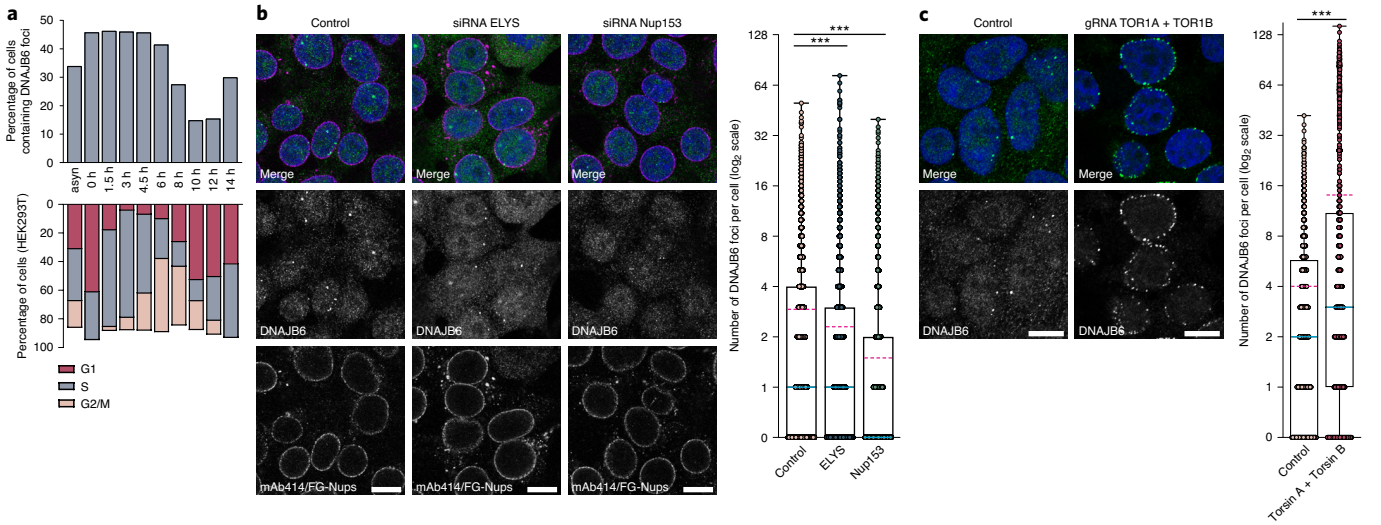

Fig. 2 | DNAJB6 foci formation is cell cycle dependent and is related to interphase NPC assembly. a, Top: percentage of DNAJB6 foci in HEK293T cells after release from cell cycle synchronization. The percentage of foci-containing cells is given for the depicted time after the release from the double thymidine block. Bottom: synchronization profile of HEK2393T cells after being synchronized in G1/S phase of the cell cycle by a double thymidine block. Asyn: asynchronous cell population. **b**, DNAJB6 foci (green) at the NE (NPC staining mAb414, magenta) upon siRNA-mediated knockdown of the Nup ELYS or Nup153. Log2 graph with box and whiskers minimum to maximum with all data points. Circles represent individual cells, showing the distribution of the amount of DNAJB6 foci per cell for the indicated siRNA treatment. Control $n = 5$ independent experiments with 8,298 cells examined, ELYS $n = 4$ independent experiments with 6,839 cells examined, Nup153 $n = 4$ independent experiments with 7,690 cells examined, automated with ICY; median is indicated with a blue solid line, and mean is indicated with a pink dashed line; unpaired *t*-test, two-tailed *P* value; $^{***}P < 0.0001$ mock versus ELYS, $^{***}P < 0.0001$ mock versus Nup153; mean ± s.e.m. **c**, HEK293T cells stained for DNAJB6 (green) under CRISPRi knockdown of Torsins A and B, with a distribution of amount of DNAJB6 foci per cell. $\log_2$ graph with box and whiskers minimum to maximum with all data points. Circles represent individual cells, showing the distribution of the amount of DNAJB6 foci. Control $n = 3$ independent experiments with 1,272 cells examined, guide RNA (gRNA) TOR1A + TOR1B $n = 3$ independent experiments with 952 cells examined, automated with ICY; median is indicated with a solid line, and mean is indicated with a dashed line; unpaired *t*-test, two-tailed *P* value; $^{***}P < 0.0001$; mean ± s.e.m. Scale bars on all fluorescent images represent 10 µm. Source numerical data are available in source data.

be revealed and include local synthesis at the NPC, co-translation of FG-Nups and nuclear transport receptor binding[12,13]. During our studies on the molecular chaperone DNAJB6, we noticed that this chaperone partially localizes to the NE, but a role at this subcellular location had not been described. DNAJB6 belongs to the large class of J domain proteins (JDPs) that function as co-chaperones of the HSP70 chaperones[14], and it has been shown to prevent aggregation of amyloidogenic substrates, including polyglutamine (polyQ)-containing proteins[15–17], amyloid-β[18], α-synuclein[19] and yeast prions[20,21]. In this Article, we provide evidence that DNAJB6 surveils FG-Nups to aid NPC assembly.

Results

DNAJB6 localizes in foci at the NE and its loss impacts NPCs

During our studies on the molecular chaperone DNAJB6, we noticed that DNAJB6 localizes not only to the nucleus and cytoplasm (Extended Data Fig. 1a) but also to specific foci at the NE (Fig. 1a), with 75% of cells having one or more foci (Fig. 1a, Extended Data Fig. 1a and Supplementary Video 1). DNAJB6 foci are not limited to HEK293T cells but are observed in multiple cell lines (Extended Data Fig. 1b). DNAJB6 foci co-localize with Lamin B1 (Fig. 1b) and are in close proximity to NPCs (Fig. 1c). To validate the DNAJB6-specific antibody, we stained DNAJB6 knockout (KO) cells and observed that the foci at the nuclear rim were absent (Fig. 1d). Strikingly, DNAJB6 KO cells contain large accumulations of NPC material in the cytoplasm (Fig. 1d,e), whereas Lamin B1 staining is unaffected (Extended Data Fig. 1c), suggesting that the NE is still intact. In addition, NPC components in wild-type (WT) cells are mostly homogeneously distributed throughout the NE, whereas they are irregularly distributed over the NE in DNAJB6 KO cells (Fig. 1d (arrows) and Extended Data Fig. 1d). Knockdown of DNAJB6 using small interfering RNA (siRNA) results in similar accumulations of NPC-positive material in the cytoplasm (Extended Data Fig. 1e), while adding back green fluorescent protein (GFP)-DNAJB6b reversed this (Extended Data Fig. 1f). Large-scale 2D transmission electron microscopy (TEM) in DNAJB6 KO cells revealed that the cytoplasmic accumulations are NPC-like structures aligned in sheets (Fig. 1f) or in strings (Extended Data Fig. 1g). NPCs in the sheets look similar to the NPCs in the NE and resemble annulate lamellae[22,23] (Fig. 1f (arrowheads) and Extended Data Fig. 1h). Single or multiple cytoplasmic NPCs are present in 83% of the imaged DNAJB6 KO cells, compared to only 5% in HEK293T WT cells. Immunofluorescence detects only larger annulate lamellae structures, hence the lower number in Fig. 1e (~30% of the cells). The NPC contains over 30 different Nups (Fig. 1g), and staining for several of them in WT and DNAJB6 KO cells indicates that the cytoplasmic NPC accumulations in DNAJB6 KO cells lack Nups from the basket, but stain positive for components of other NPC subcomplexes (Fig. 1h and Extended Data Fig. 1i). The full composition of annulate lamellae remains to be determined, but as far as currently known, all of the above is consistent with these cytoplasmic accumulations being annulate lamellae as described by others[24–28]. The appearance of annulate lamellae in somatic cycling cells has been associated with disruptions in NPC biogenesis[28,29] that can lead to disturbances in nucleocytoplasmic shuttling, including the mislocalization of RNA[9,30,31]. Indeed, DNAJB6 KO cells show a retention of RNA in the nucleoplasm (Extended Data Fig. 2a).

To see if other JDPs are also present at the NE and if their knockdown leads to the formation of annulate lamellae, we tested a subset of them using ectopically expressed GFP-tagged versions. The closely related DNAJB2 and testis-specific DNAJB8 (ref. [14]) are also found to localize at the NE where they co-localize with DNAJB6 foci (Extended Data Fig. 2b). The more dissimilar JDPs, DNAJB1 and DNAJA1 (ref. [32]), do not (Extended Data Fig. 2b). Moreover, knockdown of DNAJB2 also

https://doi.org/10.1038/s41556-022-01010-x

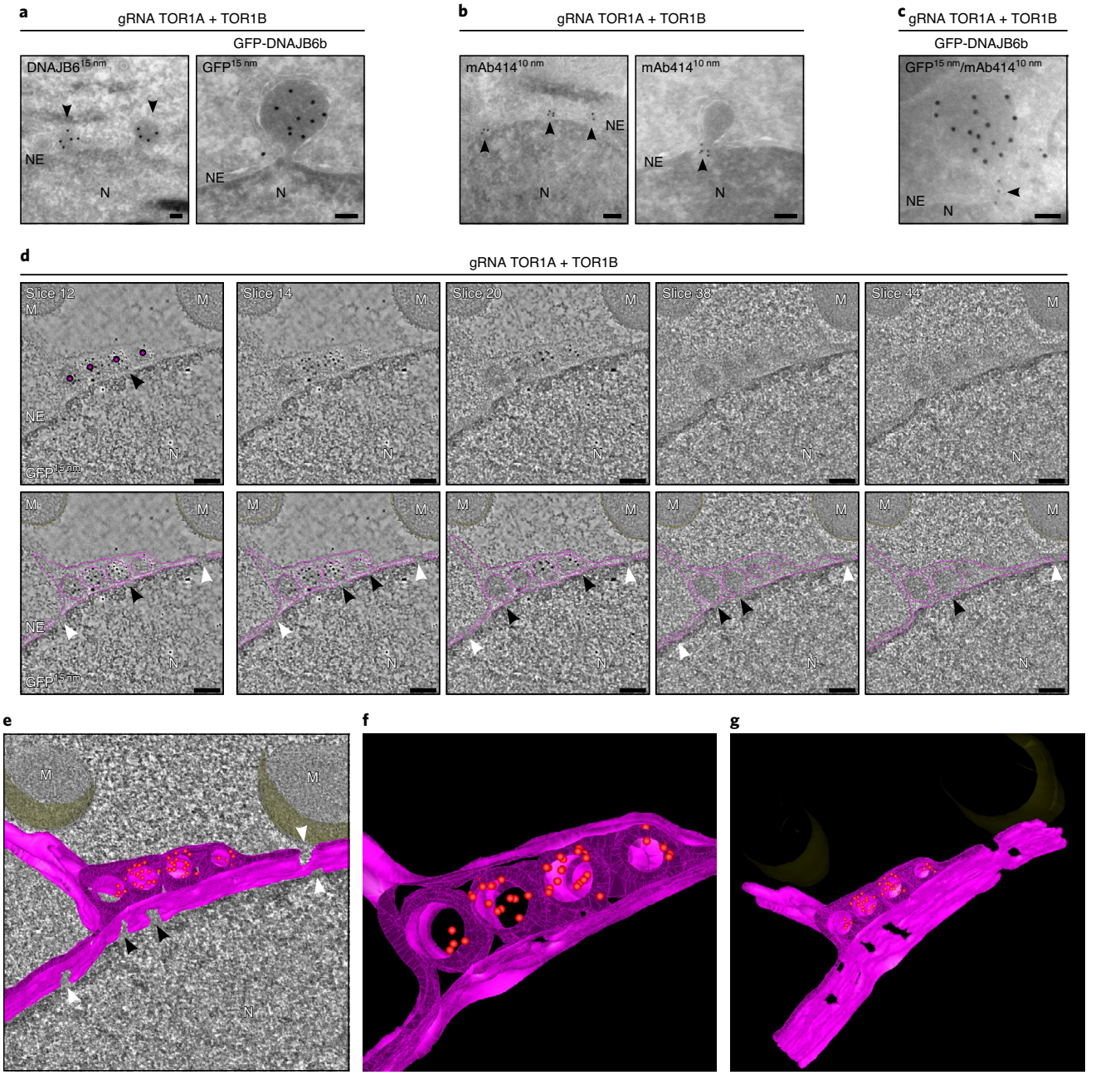

Fig. 3 | DNAJB6 localizes to herniations at the NE. a, TEM images of HEK293T cells with CRISPRi knockdown of Torsin A and Torsin B, either without expression of GFP-DNAJB6b (left, arrowheads indicate herniations) or with GFP-DNAJB6b (right), processed with Tokuyasu cryosectioning. Cryosections of 250 nm thickness were labelled with either anti-DNAJB6 or anti-GFP antibody, followed by incubation with 15 nm gold particle-conjugated protein. **b**, Cryosections were labelled with mAb414 antibody against FG-Nups, followed by incubation with 10 nm gold particle-conjugated protein A, showing clear labelling of NPCs (left). In 30% of GFP-labelled herniations, labelling can be observed at the neck of herniations (right). **c**, Double labelling of sections for GFP-DNAJB6b and FG-Nups shows proximity of DNAJB6 in a herniation to the NPC. All scale bars in **a**, **b** and **c** represent 500 nm. Nucleus is indicated with N. **d**, On immunoelectron tomography slices, surface labelling was used to select areas of interest before recording tilt series. Tomographic slice (*Z* slice 12) reveals the specific immuno-gold (15 nm) labelling on the surface of the cryosection. Asterisk indicates herniations. Indicated tomographic slices extracted from the tomogram show herniations at the NE. In the bottom images, nuclear membranes are traced (pink). More electron-dense areas can be observed at the neck of the herniations where the NE bends into the herniation, indicated by black arrowheads. NPCs are indicated with white arrowheads. Nucleus is indicated with N, and mitochondria with M. Scale bars represent 156 nm. **e**, Three-dimensional model of GFP-DNAJB6b-positive herniations were obtained by electron tomography of 400- to 450-nm-thick cryosections. NE represented in pink, and GFP gold labelling in red. Openings underneath herniations are indicated with black arrowheads, and NPCs with white arrowheads. **f**,**g**, Stills from the 3D model (Supplementary Video 3) showing a close-up of the herniations with the localization of the GFP gold labelling in red (**f**) and a view from the nuclear side where the openings of the NPCs and the herniations can be seen (**g**).

results in the formation of annulate lamellae, whereas knockdown of DNAJB1 and DNAJA1 does not (Extended Data Fig. 2c). This suggests that formation of annulate lamellae is specific to the absence of a subclass of JDPs to which DNAJB6 belongs.

DNAJB6 foci are associated with interphase NPC biogenesis

In higher eukaryotes, which have open mitosis, there are two main mechanisms of NPC biogenesis: (1) post-mitotic biogenesis when the NE and NPCs in both nuclei re-assemble after cell division, and

https://doi.org/10.1038/s41556-022-01010-x

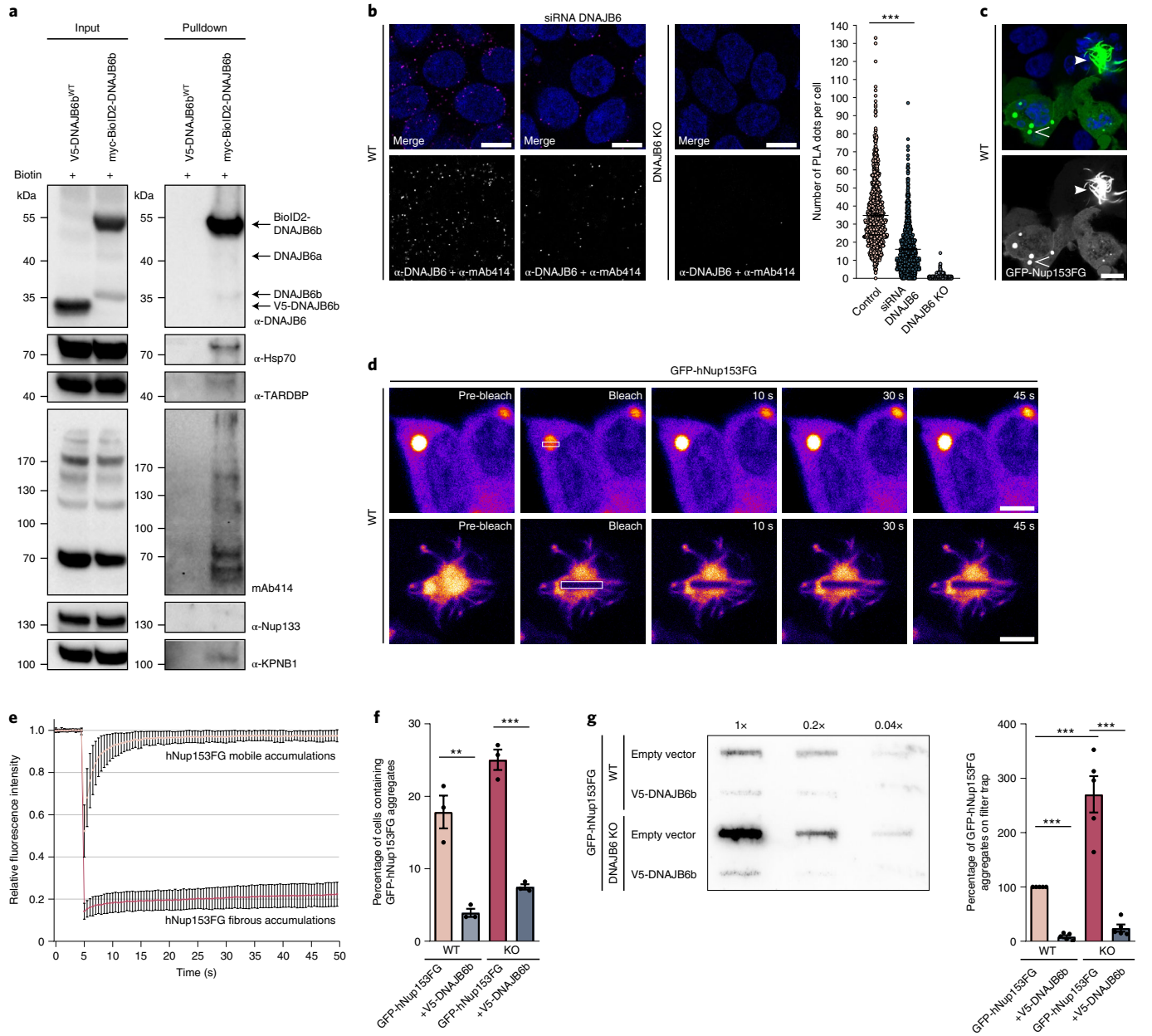

Fig. 4 | DNAJB6 interacts with FG-Nup components of the NPC. a, HEK293T cells expressing V5-DNAJB6b or BioID2-DNAJB6b, treated for 24 h with 50 µM biotin. Biotinylated close-proximity partners of DNAJB6b were pulled down by biotin affinity immunoprecipitation with streptavidin beads, run on SDS–PAGE, and Nups were detected with specific antibodies against Nup133 and mAb414. **b**, PLA detection of interaction between DNAJB6 and FG-Nups (mAb414). Graph depicts a distribution of the number of PLA dots per cell; control $n = 3$ independent experiments with 743 cells examined, siRNA DNAJB6 $n = 3$ independent experiments with 571 cells examined, DNAJB6 KO $n = 2$ independent experiments with 631 cell examined; unpaired t-test, two-tailed P value; $^{***}P < 0.0001$; mean ± s.e.m. Scale bars, 10 µm. **c**, HEK293T expressing GFP-hNup153FG show spherical accumulations (open arrowhead) and fibrous aggregates (closed arrowhead). Scale bar, 10 µm. **d**, Fluorescence images of FRAP on structures formed by GFP-Nup153FG. Spherical (mobile) structures shows quick recovery after photobleaching (mobile), whereas fluorescence of fibrous structures does not recover fluorescence in bleached areas (immobile). Scale bars, 5 µm. **e**, FRAP curves with error bars representing s.d. over three independent experiments with $n = 35$ individual cells for mobile and $n = 14$ individual cells for fibrous structures. **f**, Percentage of cells containing fibrous structures of GFP-hNup153FG in WT and DNAJB6 KO cells without and with co-overexpression of V5-DNAJB6b. $n = 3$ independent experiments; unpaired t-test, two-tailed P value; $^{**}P = 0.004$, $^{***}P = 0.0003$; mean ± s.e.m. **g**, FTA of cells with GFP-hNup153FG overexpression. Three serial five-fold dilutions were loaded onto cellulose-acetate membranes and probed with anti-GFP antibodies to detect aggregation of the GFP-hNup153FG fragment in either HEK293T WT or DNAJB6 KO cells and without or with co-overexpression of V5-DNAJB6b. Band intensities on filter trap are quantified relative to the band intensity of hNup153FG aggregation in WT HEK293T. $n = 5$ independent experiments; unpaired t-test, two-tailed P value; $^{***}P < 0.0001$ WT versus WT + DNAJB6, $^{***}P = 0.0009$ WT versus KO, $^{***}P < 0.0001$ KO versus KO + DNAJB6b; mean ± s.e.m. Source numerical data and unprocessed blots are available in source data.

(2) interphase biogenesis when new NPCs are inserted into the double membrane of the NE[3]. By synchronizing cells in G1/early S phase using a double thymidine block (Fig. 2a (bottom) and Extended Data Fig. 3a), we noted that DNAJB6 foci decrease at the start of mitosis, and foci numbers increase only when cells have progressed through mitosis and enter G1/S (Fig. 2a (top) and Extended Data Fig. 3b). Thus,

DNAJB6 foci correlate with interphase biogenesis as they appear in G1/S when NEs are re-established and post-mitotic NPC biogenesis in telophase has already been completed. To corroborate this, we knocked down the critical Nups for either post-mitotic or interphase assembly (Extended Data Fig. 3c). Knockdown of ELYS, required for the initiation of post-mitotic NPC biogenesis[33], resulted in a decrease (from 2.9 to 2.4) in the average number of DNAJB6 foci (Fig. 2b and Extended Data Fig. 3d). Knockdown of Nup153, the basket FG-Nup that is an important player in initiation of interphase NPC biogenesis[34], resulted in a stronger decrease (from 2.9 to 1.5) in the number of DNAJB6 foci at the NE (Fig. 2b and Extended Data Fig. 3e). Knockdown of ELYS as well as Nup153 also induced annulate lamellae, while knockdown of the cytoplasmic NPC component Nup358 did not (Extended Data Fig. 3f). This is in line with both ELYS and Nup153 being needed for NPC biogenesis, albeit in a different step of the cell cycle[33,34], and illustrates that here the annulate lamellae are a proxy for NPC biogenesis defects.

To further test if DNAJB6 foci are associated with (stalled) NPC intermediates, cells were depleted of Torsin A and Torsin B with clustered regularly interspaced short palindromic repeats (CRISPR) interference (CRISPRi; Extended Data Fig. 3g). Torsins are thought to be responsible for completing interphase NPC biogenesis, possibly by playing a role in inner nuclear membrane (INM)/outer nuclear membrane (ONM) fusion[35]. The functionality of Torsins depends on the interaction with the co-factors LAP1 or LULL1 (refs. [36–38]). Depletion of Torsins resulted in an increase in the number of DNAJB6 foci per cell (Fig. 2c and Extended Data Fig. 3h,i). Interestingly, ectopic expression of a mutant Torsin A that cannot interact with its co-factors (Torsin A ΔE302 (ref. [37])), and that is causative for early-onset DYT1 dystonia[39], results in an increase in DNAJB6 foci as well (Extended Data Fig. 3j). Moreover, foci induced by Torsin depletion are known to be ubiquitin positive[36] and we confirm the presence of ubiquitin in the DNAJB6 foci (Extended Data Fig. 3k). Together, these results show that DNAJB6 foci coincide with interphase NPC biogenesis and point to a role of DNAJB6 at an early stage of the process, that is, after initiation (Nup153) but before fusion of the pre-assembled cytoplasmic subcomplexes with the NE.

DNAJB6 resides in NE herniations

Stalling NPC biogenesis in interphase by knocking down Torsins leads to the formation of herniations at the NE[40] (Fig. 3a). TEM revealed that both endogenous DNAJB6 (Fig. 3a (left) and Extended Data Fig. 4a) and ectopically expressed GFP-DNAJB6b (Fig. 3a, right) localize within these herniations in 82% and 94% of herniations analysed, respectively. At the neck of the herniations, a structure reminiscent of the NPC is recurrently observed[35,41]. FG-Nups, labelled with mAb414 antibody, localize to NPCs that are embedded in the NE (Fig. 3b, left), and occasionally to the neck of the herniations (Fig. 3b, right). Double labelling for mAb414 (10 nm gold) and GFP (15 nm gold) confirms the localization of NPC components with DNAJB6 at herniations (Fig. 3c), and around a quarter of the herniations that were positive for DNAJB6 or GFP-DNAJB6b were also labelled with the mAb414 antibody. Herniations have also been suggested to carry specific cargo[42,43], and in a recent study it was indeed shown that the content is not random, as no canonical Endoplasmatic-Reticulum Associated Degradation[41] and no nuclear transport or ribosome components[35] were found inside them. Importantly, DNAJB6, DNAJB2 and other HSP70 machinery proteins were identified in a mass spectrometry analysis of NEs isolated from Torsin-depleted cells[35]. In that study[35], myeloid leukemia factor 2 (MLF2) and ubiquitin were also identified as major components of herniations. Consistently, we find HSP70 (HSPA1A), ubiquitin and MLF2 to co-localize with DNAJB6 foci at the NE (Extended Data Fig. 4b,c).

Next, we used immunoelectron tomography on Tokuyasu thick cryosections[44] to obtain insight in the 3D organization of the DNAJB6-containing herniations. The herniations (Fig. 3d, indicated with asterisks on slice 12) were located in the cell sections by immuno-gold labelling using GFP antibody (Fig. 3d) or an antibody against DNAJB6 (Extended Data Fig. 4a and Supplementary Video 2). Subsequent *Z*-slices obtained through the tomography of the GFP-DNAJB6b-positive herniations reveal that the double membrane of the NE continues into the membrane around the herniation (Fig. 3d,e and Supplementary Video 3). On some occasions, several individual INM herniations are enclosed by a single ONM. The INM surrounding these individual herniations were never found to be fused with INMs of other herniations (Fig. 3d,f). Recently, herniations with NPC-resembling structures at the cytoplasmic side have been described to occur under starvation conditions, and were proposed to involve NPC turnover[45]. From the tomography it becomes evident that the ONM of the herniations does not have openings and is continuous with the endoplasmic reticulum (ER; Fig. 3d and Supplementary Video 3). In addition, starvation did not induce DNAJB6 foci formation (data not shown). These two findings suggest that the DNAJB6-containing herniations are not related to (starvation-induced) NPC turnover. Our data are in line with a role of DNAJB6 in interphase NPC biogenesis since the 3D model of the DNAJB6-containing herniations clearly shows that there are only openings underneath the herniations at the NE (Fig. 3d (black arrows) and g). At the neck, it contains a more electron-dense structure with similar dimensions as NPCs in the NE (Fig. 3d,e). Together with the NPC labelling (Fig. 3b,c), this suggests that NPC material is present at the neck of the herniations and is in line with the presence of an NPC biogenesis intermediate[41].

Treating the cells with the aliphatic alcohol 1,6-hexanediol, which is known to disrupt the permeability barrier of the NPC in vivo[46] and to disrupt liquid–liquid phase interactions of FG-Nups in vitro[47], almost immediately leads to a loss of DNAJB6 foci at the NE (Extended Data Fig. 4d). DNAJB6 foci largely remained after treatment with 2,5-hexanediol, which has little effect on the melting of FG domain condensates (Extended Data Fig. 4d). This may indicate that 1,6-hexanediol permeabilizes the NPCs after which DNAJB6 exits on the nuclear side from the herniations. We speculate that, when INM/ONM fusion is stalled, herniations are formed that contain DNAJB6, and possibly other factors involved in NPC biogenesis. These factors would normally have been released into the cytoplasm if NPC biogenesis and fusion of INM/ONM would proceed as usual[42] through an inside-out mechanism[48,41].

DNAJB6 interacts with FG-Nups and prevents their aggregation

The presence of DNAJB6 at sites for NPC biogenesis could reflect the ability of this chaperone to specifically prevent FG-Nups to undergo unwanted interactions, and possibly even aggregate[7], during biogenesis. By using a BioID2-DNAJB6b fusion construct (Extended Data Fig. 5a,b), FG-Nups detected using mAb414 and importin β could be identified as close-proximity partners of DNAJB6b, but not Nup133, a component of the outer ring complex and not an FG-Nup (Fig. 4a). To directly monitor the interaction of DNAJB6 with FG-Nups in situ, we used proximity ligation assay (PLA). The PLA shows that DNAJB6 and FG-Nups interact at the NE, as well as in the cytosol (Fig. 4b), consistent with our findings that DNAJB6 is required in a step after initiation (Nup153) but before fusion of the pre-assembled cytoplasmic subcomplexes with the NE. Knockdown of DNAJB6 leads to a significant reduction of PLA dots, and in DNAJB6 KO cells (Fig. 4b) and control conditions (Extended Data Fig. 5c), PLA signal is almost undetectable, confirming the signal specificity.

Next, we investigated more directly if the chaperone function of DNAJB6 affects the condensation or aggregation behaviour of FG-Nups. In vitro, in silico and in vivo work previously showed that the phase separation and aggregation propensity of FG-Nups is dependent on the interaction between the phenylalanine residues in the FG-repeat regions and is tuned by the specific amino acids surrounding the FG-repeats[49–51]. To test if DNAJB6 can alter the condensation properties of FG-Nups, we started with Nup153 as it is a key FG-Nup in initiating interphase biogenesis[34], and it is implicated in DNAJB6 foci formation

https://doi.org/10.1038/s41556-022-01010-x

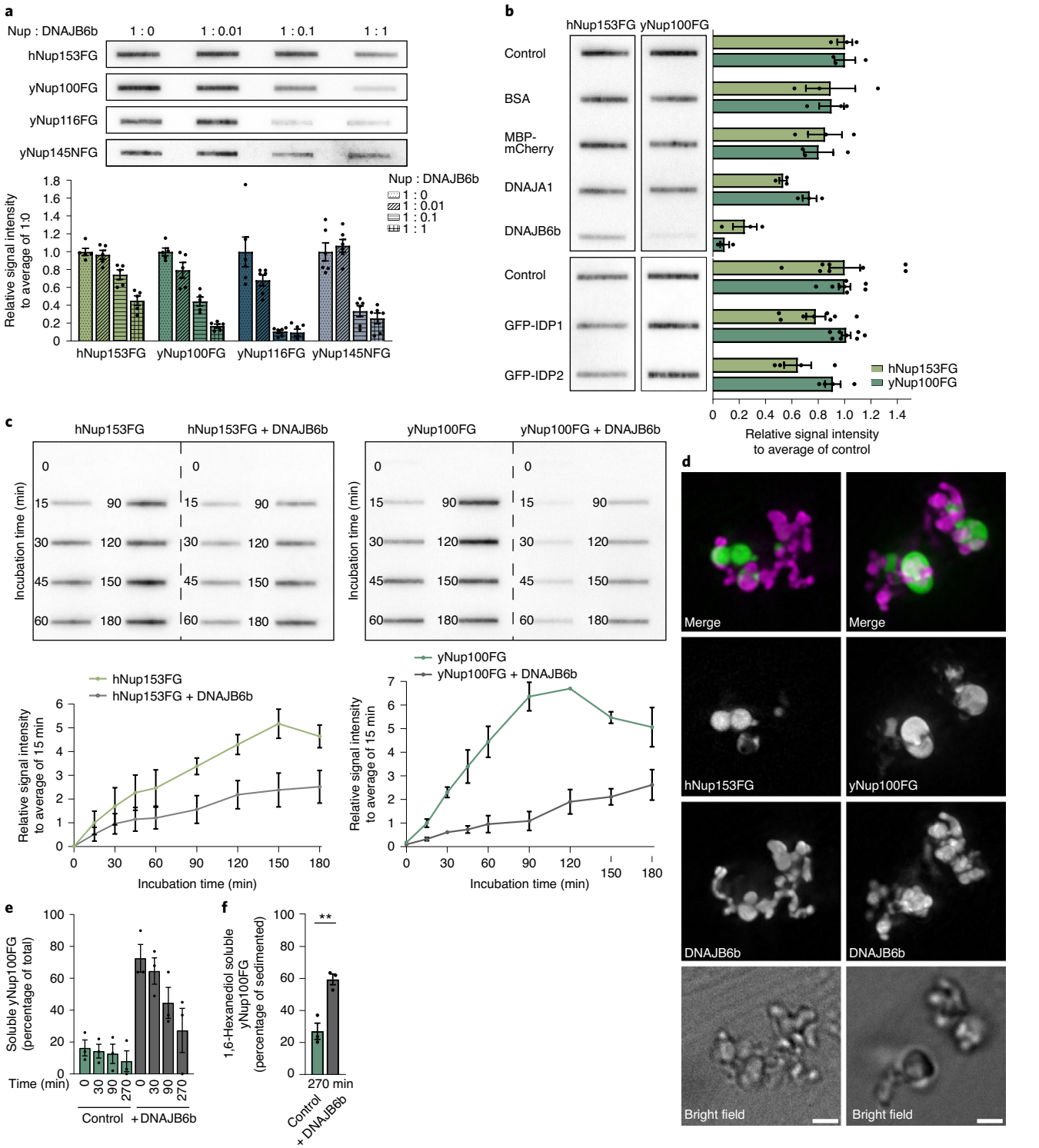

Fig. 5 | DNAJB6b modulates the LLPS and aggregation of FG-Nup fragments in vitro. a, FTA to detect aggregation of purified FG-Nup fragments, hNup153FG (6 µM), yNup100FG (6 µM), yNup116FG (3 µM) and yNup145N (3 µM), in the absence (control) and presence of the indicated molar ratios of DNAJB6b. Band intensities on filter trap are quantified relative to the average intensity in the absence of DNAJB6b. hNup153FG and yNup100FG $n = 5$ independent experiments, yNup116FG and yNup145N $n = 6$ independent experiments; mean ± s.e.m. **b**, As in **a**, purified hNup153FG or yNup100FG were incubated in the absence (control) or presence of BSA, MBP-mCherry, DNAJA1, DNAJB6b (all $n = 3$ independent experiments), GFP-tagged IDP1 ($n = 8$ independent experiments) or GFP-tagged IDP2 ($n = 4$ independent experiments) at a molar ratio of 1:1. Mean ± s.e.m. **c**, As in **a**, time-dependent formation of hNup153FG and yNup100FG aggregates in the absence and presence of DNAJB6b at a molar ratio of 1:1. Graphs below depict quantifications; $n = 3$ independent experiments; mean ± s.e.m. **d**, Fluorescence and bright field microscopy images showing co-localization of fluorescein-labelled hNup153FG and yNup100FG with Texas-red-labelled DNAJB6b at a molar ratio of 1:1. Scale bar represents 2 µm. **e**, Sedimentation assay assessing the soluble fraction of yNup100FG incubated with or without DNAJB6b at a molar ratio of 1:0.5 for the indicated times. **f**, As in **e**, but now to determine the fraction 1,6-hexanediol soluble condensates, 10% 1,6-hexanediol was added for 10 min before centrifugation. $n = 3$ independent experiments; unpaired *t*-test, two-tailed *P* value; $^{**}P = 0.0061$; mean ± s.e.m. Individual replicates are shown in Extended Data Figs. 6–9; source numerical data and unprocessed blots are available in source data.

https://doi.org/10.1038/s41556-022-01010-x

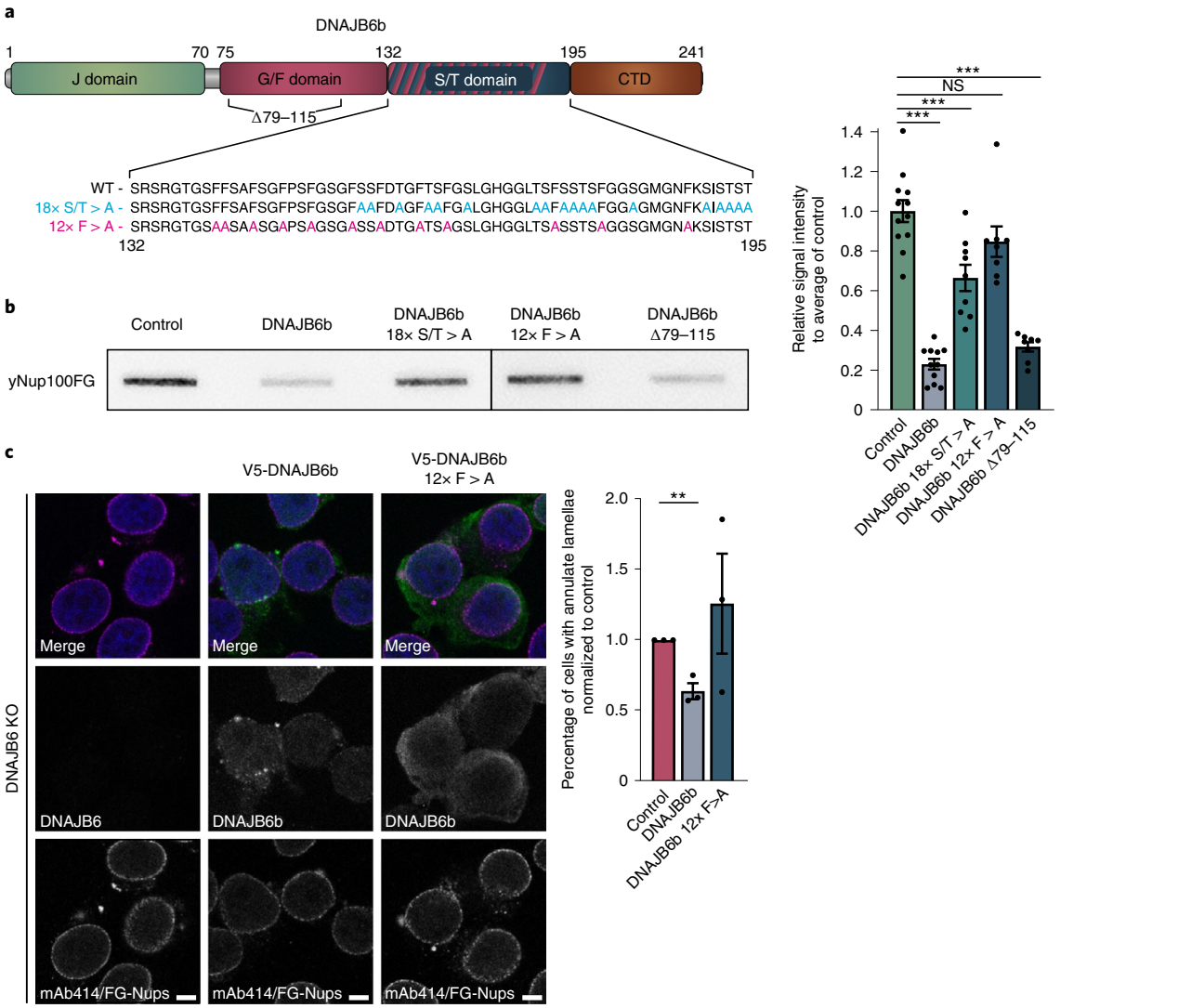

Fig. 6 | The S/T domain of DNAJB6 mediates the interaction with FG-Nups. **a**, Schematic overview of the domain structure of DNAJB6b, indicating the N-terminal J domain (green), followed by the G/F domain (pink), the S/T domain (blue) and the C-terminal domain (CTD) (brown). The locations of the different mutations (18× S/T > A, 12× F > A) and deletion (Δ79–115) are indicated. **b**, FTA showing the effect of WT or indicated DNAJB6b mutants (18× S/T > A, 12× F > A, Δ79–115) on the aggregation of yNup100FG (molar ratio 1:1). Band intensities on filter trap are quantified relative to the average intensity in the absence of DNAJB6b. Control ($n = 12$ independent experiments), DNAJB6b ($n = 11$;$^{***}P < 0.0001$), 18× S/T > A ($n = 9$ independent experiments; $^{***}P = 0.0009$), 12× F > A ($n = 8$ independent experiments; $P = 0.119$ (NS, not significant)), Δ79–115 ($n = 8$ independent experiments; $^{***}P < 0.0001$); unpaired *t*-test, two-tailed *P* value; mean ± s.e.m. **c**, Overexpression of DNAJB6b WT in DNAJB6 KO cells shows partial rescue of annulate lamellae. Overexpression of DNAJB6b 12× F > A does not rescue the accumulation of annulate lamellae. Scale bars, 5 µm. Graph depicts relative percentage of cells containing annulate lamellae. $n = 3$ independent experiments; unpaired *t*-test, two-tailed *P* value; $^{**}P = 0.0031$; mean ± s.e.m. Individual replicates are shown in Extended Data Fig. 9; source numerical data and unprocessed blots are available in source data.

(Fig. 2b). For this, the FG region of the human Nup153 (hNup153FG) tagged with GFP was overexpressed in HEK293T cells (Fig. 4c), which did not elicit a cellular stress response (Extended Data Fig. 5d). In contrast to full-length Nup153, which predominantly localizes at NPCs (Extended Data Fig. 5e), expression of the FG-Nup fragment lacking the NPC anchoring domain (hNup153FG) leads to the formation of artificial cytosolic assemblies. These can be used to probe the activity of DNAJB6 in cells. Two categories of GFP-hNup153FG accumulations can be distinguished: smaller spherical and larger fibrous structures (Fig. 4c). The ability to form such accumulations is specifically related to the presence of the FG-repeats as GFP-hNup153AG—a mutant in which all phenylalanines have been replaced with alanines—does not form accumulations of any kind[7] (Extended Data Fig. 5f). The different accumulations found for hNup153FG have distinct properties. The spherical accumulations can be characterized as mobile as they show quick fluorescence recovery after photobleaching (FRAP) (Fig. 4d,e). Within these accumulations, fluorescence is quickly redistributed after bleaching and fluorescence is even regained almost back to pre-bleached levels, suggesting exchange with its surroundings. However, the larger fibrous structures do not recover from photobleaching and have a more solid character (Fig. 4d,e).

DNAJB6 co-localizes with the hNup153FG structures (Extended Data Fig. 5g), and more importantly, the percentage of cells with large fibrous structures increases in a DNAJB6 KO background, while the formation of fibrous structures is almost completely suppressed upon DNAJB6b overexpression or re-expression (Fig. 4f). In addition, a small fraction of hNup153FG is 0.5% sodium dodecyl-sulfate (SDS) insoluble and is retained on 0.2 µm pore size cellulose acetate filters (Fig. 4g). Similar to what we find for the larger fibrous structures, the amount of SDS-insoluble material of hNup153FG increases in DNAJB6 KO cells and

is reduced upon DNAJB6 overexpression (Fig. 4g) and strictly depends on the FG motifs, as the GFP-hNup153AG mutant is not retained on the cellulose acetate filters after SDS extraction (Extended Data Fig. 5h), as was shown before[7]. Moreover, the association between hNup153FG and DNAJB6 (Extended Data Fig. 5i, last lane) also specifically depends on the presence of the FG motifs (Extended Data Fig. 5i, middle lane).

DNAJB6 modulates the phase state of FG-Nup domains in vitro

The propensity to phase-separate into particles has been studied already for diverse FG-Nups from yeast and human NPCs[5–7,50,52–54]. Their propensity to phase separate into particles depends on the unique features of each FG-Nups sequence. For example, the FG region of yeast Nup100 as purified from *Escherichia coli* is rather cohesive and has a particularly high propensity to form condensates[52], and the FG region of hNup153 is even able to transition into amyloid-like structures[7]. To test if DNAJB6 is directly responsible for the anti-aggregation effects on FG-Nups, we purified DNAJB6b and assessed its effects on the behaviour of the purified FG regions of human Nup153 (hNup153FG), as well as yeast Nup100 (yNup100FG), Nup116 (yNup116FG) and Nup145N (yNup145NFG). Recombinant hNup153FG becomes insoluble, depending on the crowding reagent used, and can be trapped on a filter trap, indicating it is aggregated (Extended Data Fig. 6a). Importantly, adding recombinant DNAJB6b reduces the aggregation of hNup153FG in a dose-dependent manner (Fig. 5a and Extended Data Fig. 6b). yNup100FG, yNup116FG and yNup145NFG form aggregates as well, and this aggregation is also strongly reduced in the presence of DNAJB6b (Fig. 5a and Extended Data Fig. 6c–e). The anti-aggregation activity of DNAJB6b is specific, as neither BSA, MBP-mCherry, DNAJA1 nor two intrinsically disordered proteins (IDPs)[55,56] influence the aggregation of either hNup153FG or yNup100FG (Fig. 5b and Extended Data Fig. 7a–d). In the presence of DNAJB6b, the aggregation of both hNup153FG and yNup100FG is delayed from the start (Fig. 5c and Extended Data Fig. 8a, b), suggesting it acts early in the transition, in line with the effect on preventing amyloid formation of polyQ-containing proteins[16] and Aβ1-42 (refs. [57,58]).

It is known that before aggregation FG-Nups undergo phase state changes, and therefore, we addressed whether DNAJB6b can also alter the phase state of FG-Nups. In our assay conditions, DNAJB6 forms microscopically visible assemblies that are SDS soluble but 1,6-hexanediol insoluble, suggesting they are gel-like condensates (Extended Data Fig. 9a). This condensation behaviour is in line with earlier findings showing that DNAJB6b forms polydisperse complexes[59,60]. When Texas-red-labelled DNAJB6b and fluorescein-5-labelled hNup153FG or yNup100FG are mixed, they co-localize in condensating bodies (Fig. 5d). Unlabelled DNAJB6b also co-localizes in condensating bodies with the FG-repeat fragments (Extended Data Fig. 9b). To quantify the impact of DNAJB6b on the formation of FG-repeat condensates, we performed sedimentation assays with yNup100FG. The presence of DNAJB6b ensures that a larger fraction of Nup100FG remains soluble over longer timeframes (Fig. 5e and Extended Data Fig. 9c). Moreover, in the presence of DNAJB6b a larger fraction of yNup100FG remained in a 1,6-hexanediol soluble state after prolonged incubation (Fig. 5f and Extended Data Fig. 9c), suggesting that DNAJB6b delays the transition of yNup100FG from a liquid-like to a more solid-like state.

The S/T domain is required for the DNAJB6 FG-Nup interaction

The anti-aggregation activity of DNAJB6 on amyloidogenic substrates, including polyQ proteins and amyloid-β, depends on the serine and threonine-rich C-terminal domain (S/T domain). Upon replacement of the 18 serines and threonines in this domain for alanines (18× S/T > A) (Fig. 6a), DNAJB6 loses its anti-amyloidogenic activity[16]. We tested this mutant and find it is also partly impaired in its activity to prevent the formation of FG-repeat aggregates (Fig. 6b and Extended Data Fig. 9d). A mutant version of DNAJB6 found in patients with limb-girdle muscular dystrophy lacks a large part of the more N-terminal G/F domain of DNAJB6b (Δ79–115)[61]. We find that this mutant can still suppress FG-Nup aggregation (Fig. 6b). Interestingly, the S/T domain is rich in phenylalanines and glycines, resembling the FG regions of the FG-Nups (Supplementary Table 1)[62]. We thus mutated the 12 phenylalanines in the S/T domain to alanines (12× F > A) (Fig. 6a) and find it is unable to prevent aggregation of yNup100FG (Fig. 6b). We then tested this F > A mutant in cells and, gratifyingly, the DNAJB6b 12× F > A mutant is also unable to prevent the formation of annulate lamellae in DNAJB6 KO cells, while WT DNAJB6b does suppress annulate lamellae (Fig. 6c).

Discussion

Altogether, our data show that the molecular chaperone DNAJB6 plays a prominent role in interphase NPC biogenesis. To our knowledge, chaperones of the heat shock protein network had not previously been implicated in this process. Compromising DNAJB6 leads to disturbed NPC biogenesis, leading to the accumulation of annulate lamellae and problems in RNA transport. When interphase NPC biogenesis process is stalled, DNAJB6 (and other components of the HSP70 chaperone network) ends up in the resulting herniation at the NE. It is likely that, if NPC biogenesis proceeds normally, the early interactors, including DNAJB6, of these NPC assembly intermediates are released at the cytoplasmic side of the NPC. We show that DNAJB6 by itself protects the natively disordered FG region of FG-Nups from transitioning from a liquid to a more solid state, through interactions by phenylalanines in its S/T domain.

In a parallel paper by the Schlieker group, the herniation co-resident MLF2 was also identified to act on the FG-Nups by modulating their interactions[63]. These herniations can be induced by deletion or mutation of Torsin A[64,65]; the latter is also causative for DYT1 dystonia (Torsin A ΔE302/3). The activity of DNAJB6 towards native FG-Nups is similar to its previously described anti-aggregation activity on mutant disease-related protein substrates, including polyQ-containing proteins[15–17], and α-synuclein[19], some of which have been suggested to be disordered as well. This makes DNAJB6 a chaperone for IDPs in normal cellular physiology, as well as in disease. DNAJB6 mutations are causative for limb-girdle muscular dystrophy[66], and surveillance of intrinsically disordered polypeptides may be important for this disease as well. Many of the DNAJB6 substrates relate to neurodegenerative diseases[15–17,21,58], and several are also characterized by disturbances in NPCs and/or nucleocytoplasmic transport[9,67–72], similar to what we find as a result of DNAJB6 depletion. This suggests an intriguing link between the heat shock protein chaperone network, nuclear transport receptors, ageing-related aggregation-prone proteins, and NPC assembly and function.

Online content

Any methods, additional references, Nature Research reporting summaries, source data, extended data, supplementary information, acknowledgements, peer review information; details of author contributions and competing interests; and statements of data and code availability are available at https://doi.org/10.1038/s41556-022-01010-x.

References

1. Fernandez-Martinez, J. & Rout, M. P. One ring to rule them all? Structural and functional diversity in the nuclear pore complex. *Trends Biochem. Sci.* **46**, 595–607 (2021).
2. Hampoelz, B., Andres-Pons, A., Kastritis, P. & Beck, M. Structure and assembly of the nuclear pore complex. *Annu. Rev. Biophys.* **48**, 515–536 (2019).
3. Otsuka, S. & Ellenberg, J. Mechanisms of nuclear pore complex assembly—two different ways of building one molecular machine. *FEBS Lett.* **592**, 475–488 (2018).
4. Dultz, E., Wojtynek, M., Medalia, O. & Onischenko, E. The nuclear pore complex: birth, life, and death of a cellular behemoth. *Cells* **11**, 1456 (2022).

5. Frey, S., Richter, R. P. & Görlich, D. FG-rich repeats of nuclear pore proteins form a three-dimensional meshwork with hydrogel-like properties. *Science* **314**, 815–817 (2006).
6. Schmidt, H. B. & Görlich, D. Transport selectivity of nuclear pores, phase separation, and membraneless organelles. *Trends Biochem. Sci.* **41**, 46–61 (2016).
7. Milles, S. et al. Facilitated aggregation of FG nucleoporins under molecular crowding conditions. *EMBO Rep.* **14**, 178–183 (2013).
8. D'Angelo, M. A., Raices, M., Panowski, S. H. & Hetzer, M. W. Age-dependent deterioration of nuclear pore complexes causes a loss of nuclear integrity in postmitotic cells. *Cell* **136**, 284–295 (2009).
9. Gasset-Rosa, F. et al. Polyglutamine-expanded huntingtin exacerbates age-related disruption of nuclear integrity and nucleocytoplasmic transport. *Neuron* **94**, 48–57.e4 (2017).
10. Rempel, I. L. et al. Age-dependent deterioration of nuclear pore assembly in mitotic cells decreases transport dynamics. *eLife* **8**, 1–26 (2019).
11. Larrieu, D. et al. Inhibition of the acetyltransferase NAT10 normalizes progeric and aging cells by rebalancing the Transportin-1 nuclear import pathway. *Sci. Signal* **11**, 1–16 (2018).
12. Lautier, O. et al. Co-translational assembly and localized translation of nucleoporins in nuclear pore complex biogenesis. *Mol. Cell* **81**, 2417–2427.e5 (2021).
13. Seidel, M. et al. Co-translational assembly orchestrates competing biogenesis pathways. *Nat. Commun.* **13**, 1224 (2022).
14. Kampinga, H. H. & Craig, E. A. The HSP70 chaperone machinery: J proteins as drivers of functional specificity. *Nat. Rev. Mol. Cell Biol.* **11**, 579–592 (2010).
15. Hageman, J. et al. A DNAJB chaperone subfamily with HDAC-dependent activities suppresses toxic protein aggregation. *Mol. Cell* **37**, 355–369 (2010).
16. Kakkar, V. et al. The S/T-rich motif in the DNAJB6 chaperone delays polyglutamine aggregation and the onset of disease in a mouse model. *Mol. Cell* **62**, 272–283 (2016).
17. Thiruvalluvan, A. et al. DNAJB6, a key factor in neuronal sensitivity to amyloidogenesis. *Mol. Cell* **78**, 346–358.e9 (2020).
18. Månsson, C. et al. DNAJB6 is a peptide-binding chaperone which can suppress amyloid fibrillation of polyglutamine peptides at substoichiometric molar ratios. *Cell Stress Chaperones* **19**, 227–239 (2014).
19. Aprile, F. A. et al. The molecular chaperones DNAJB6 and Hsp70 cooperate to suppress α-synuclein aggregation. *Sci. Rep.* **7**, 1–11 (2017).
20. Reidy, M., Sharma, R., Roberts, B. L. & Masison, D. C. Human J-protein DnaJB6b cures a subset of *Saccharomyces cerevisiae* prions and selectively blocks assembly of structurally related amyloids. *J. Biol. Chem.* **291**, 4035–4047 (2016).
21. Stein, K. C., Bengoechea, R., Harms, M. B., Weihl, C. C. & True, H. L. Myopathy-causing mutations in an HSP40 chaperone disrupt processing of specific client conformers. *J. Biol. Chem.* **289**, 21120–21130 (2014).
22. Kessel, R. G. Annulate lamellae: a last frontier in cellular organelles. *Int. Rev. Cytol.* **133**, 43–120 (1992).
23. Kessel, R. G. The structure and function of annulate lamellae: porous cytoplasmic and intranuclear membranes. *Int. Rev. Cytol.* **82**, 181–303 (1983).
24. Walther, T. C. et al. The conserved Nup107-160 complex is critical for nuclear pore complex assembly. *Cell* **113**, 195–206 (2003).
25. Hampoelz, B. et al. Pre-assembled nuclear pores insert into the nuclear envelope during early development. *Cell* **166**, 664–678 (2016).
26. Cordes, V. C., Reidenbach, S. & Franke, W. W. Cytoplasmic annulate lamellae in cultured cells: composition, distribution, and mitotic behavior. *Cell Tissue Res* **284**, 177–191 (1996).
27. Makio, T. et al. The nucleoporins Nup170p and Nup157p are essential for nuclear pore complex assembly. *J. Cell Biol.* **185**, 459–473 (2009).
28. Wu, X. et al. Disruption of the FG nucleoporin Nup98 causes selective changes in nuclear pore complex stoichiometry and function. *Proc. Natl Acad. Sci. USA* **98**, 3191–3196 (2001).
29. Walther, T. C. et al. RanGTP mediates nuclear pore complex assembly. *Nature* **424**, 689–694 (2003).
30. Yannarell, A., Schumm, D. E. & Webb, T. E. Age-dependence of nuclear RNA processing. *Mech. Ageing Dev.* **6**, 259–264 (1977).
31. Freibaum, B. D. et al. GGGGCC repeat expansion in C9orf72 compromises nucleocytoplasmic transport. *Nature* **525**, 129–133 (2015).
32. Kampinga, H. H. et al. Function, evolution, and structure of J-domain proteins. *Cell Stress Chaperones* **24**, 7–15 (2019).
33. Doucet, C. M., Talamas, J. A. & Hetzer, M. W. Cell cycle-dependent differences in nuclear pore complex assembly in metazoa. *Cell* **141**, 1030–1041 (2010).
34. Vollmer, B. et al. Nup153 recruits the Nup107-160 complex to the inner nuclear membrane for interphasic nuclear pore complex assembly. *Dev. Cell* **33**, 717–728 (2015).
35. Rampello, A. J. et al. Torsin ATPase deficiency leads to defects in nuclear pore biogenesis and sequestration of MLF2. *J. Cell Biol.* **219**, e201910185 (2020).
36. Chase, A. R. et al. Dynamic functional assembly of the Torsin AAA+ ATPase and its modulation by LAP1. *Mol. Biol. Cell* **28**, 2765–2772 (2017).
37. Zhao, C., Brown, R. S. H., Chase, A. R., Eisele, M. R. & Schlieker, C. Regulation of Torsin ATPases by LAP1 and LULL1. *Proc. Natl Acad. Sci. USA* **110**, E1545–E1554 (2013).
38. Esra Demircioglu, F., Sosa, B. A., Ingram, J., Ploegh, H. L. & Schwartz, T. U. Structures of torsinA and its disease-mutant complexed with an activator reveal the molecular basis for primary dystonia. *eLife* **5**, 1–14 (2016).
39. Ozelius, L. J. et al. The early-onset torsion dystonia gene (DYT1) encodes an ATP-binding protein. *Nat. Genet.* **17**, 40–48 (1997).
40. Laudermilch, E. & Schlieker, C. Torsin ATPases: structural insights and functional perspectives. *Curr. Opin. Cell Biol.* **40**, 1–7 (2016).
41. Laudermilch, E. et al. Dissecting Torsin/cofactor function at the nuclear envelope: a genetic study. *Mol. Biol. Cell* **27**, 3964–3971 (2016).
42. Szöllösi, M. S. & Szöllösi, D. 'Blebbing' of the nuclear envelope of mouse zygotes, early embryos and hybrid cells. *J. Cell Sci.* **91**, 257–267 (1988).
43. Speese, S. D. et al. Nuclear envelope budding enables large ribonucleoprotein particle export during synaptic Wnt signaling. *Cell* **149**, 832–846 (2012).
44. Slot, J. W. & Geuze, H. J. Cryosectioning and immunolabeling. *Nat. Protoc.* **2**, 2480–2491 (2007).
45. Allegretti, M. et al. In-cell architecture of the nuclear pore and snapshots of its turnover. *Nature* **586**, 796–800 (2020).
46. Shulga, N. & Goldfarb, D. S. Binding dynamics of structural nucleoporins govern nuclear pore complex permeability and may mediate channel gating. *Mol. Cell. Biol.* **23**, 534–542 (2003).
47. Shi, K. Y. et al. Toxic PRn poly-dipeptides encoded by the C9orf72 repeat expansion block nuclear import and export. *Proc. Natl Acad. Sci. USA* **114**, E1111–E1117 (2017).
48. Otsuka, S. et al. Nuclear pore assembly proceeds by an inside-out extrusion of the nuclear envelope. *eLife* **5**, 1–23 (2016).
49. Terry, L. J. & Wente, S. R. Flexible gates: dynamic topologies and functions for FG nucleoporins in nucleocytoplasmic transport. *Eukaryot. Cell* **8**, 1814–1827 (2009).
50. Yamada, J. et al. A bimodal distribution of two distinct categories of intrinsically disordered structures with separate functions in FG nucleoporins. *Mol. Cell. Proteom.* **9**, 2205–2224 (2010).

51. Huang, K., Tagliazucchi, M., Park, S. H., Rabin, Y. & Szleifer, I. Nanocompartmentalization of the nuclear pore lumen. *Biophys. J.* **118**, 219–231 (2020).
52. Schmidt, H. B. & Görlich, D. Nup98 FG domains from diverse species spontaneously phase-separate into particles with nuclear pore-like permselectivity. *eLife* **4**, 1–30 (2015).
53. Celetti, G. et al. The liquid state of FG-nucleoporins mimics permeability barrier properties of nuclear pore complexes. *J. Cell Biol.* **219**, e201907157 (2019).
54. Konishi, H. A. & Yoshimura, S. H. Interactions between non-structured domains of FG- and non-FG-nucleoporins coordinate the ordered assembly of the nuclear pore complex in mitosis. *FASEB J.* **34**, 1532–1545 (2020).
55. Meinema, A. C. et al. Long unfolded linkers facilitate membrane protein import through the nuclear pore complex. *Science* **333**, 90–93 (2011).
56. Rempel, I. L. et al. Flexible and extended linker domains support efficient targeting of heh2 to the inner nuclear membrane. *Structure* **28**, 185–195.e5 (2020).
57. Månsson, C. et al. Conserved S/T residues of the human chaperone DNAJB6 are required for effective inhibition of Aβ42 amyloid fibril formation. *Biochemistry* **57**, 4891–4892 (2018).
58. Månsson, C. et al. Interaction of the molecular chaperone DNAJB6 with growing amyloid-β 42 (Aβ42) aggregates leads to sub-stoichiometric inhibition of amyloid formation. *J. Biol. Chem.* **289**, 31066–31076 (2014).
59. Söderberg, C. A. G. et al. Structural modelling of the DNAJB6 oligomeric chaperone shows a peptide-binding cleft lined with conserved S/T-residues at the dimer interface. *Sci. Rep.* **8**, 1–15 (2018).
60. Karamanos, T. K., Tugarinov, V. & Clore, G. M. Unraveling the structure and dynamics of the human DNAJB6b chaperone by NMR reveals insights into Hsp40-mediated proteostasis. *Proc. Natl Acad. Sci. USA* **116**, 21529–21538 (2019).
61. Ruggieri, A. et al. Complete loss of the DNAJB6 G/F domain and novel missense mutations cause distal-onset DNAJB6 myopathy. *Acta Neuropathol. Commun.* **3**, 44 (2015).
62. Cascarina, S. M., King, D. C., Osborne Nishimura, E. & Ross, E. D. LCD-Composer: an intuitive, composition-centric method enabling the identification and detailed functional mapping of low-complexity domains. *NAR Genom. Bioinform* **3**, 1–19 (2021).
63. Prophet, S. M. et al. Atypical nuclear envelope condensates linked to neurological disorders reveal nucleoporin-directed chaperone activities. *Nat. Cell Biol.* https://doi.org/10.1038/s41556-022-01001-y (2022).
64. Kim, C. E., Perez, A., Perkins, G., Ellisman, M. H. & Dauer, W. T. A molecular mechanism underlying the neural-specific defect in torsinA mutant mice. *Proc. Natl Acad. Sci. USA* **107**, 9861–9866 (2010).
65. Tanabe, L. M., Liang, C. C. & Dauer, W. T. Neuronal nuclear membrane budding occurs during a developmental window modulated by torsin paralogs. *Cell Rep.* **16**, 3322–3333 (2016).
66. Ruggieri, A. et al. DNAJB6 myopathies: focused review on an emerging and expanding group of myopathies. *Front Mol. Biosci.* **3**, 63 (2016).
67. Sheffield, L. G., Miskiewicz, H. B., Tannenbaum, L. B. & Mirra, S. S. Nuclear pore complex proteins in Alzheimer disease. *J. Neuropathol. Exp. Neurol.* **65**, 45–54 (2006).
68. Eftekharzadeh, B. et al. Tau protein disrupts nucleocytoplasmic transport in Alzheimer's disease. *Neuron* **99**, 925–940.e7 (2018).
69. Grima, J. C. et al. Mutant huntingtin disrupts the nuclear pore complex. *Neuron* **94**, 93–107.e6 (2017).
70. Li, N. & Lagier-Tourenne, C. Nuclear pores: the gate to neurodegeneration. *Nat. Neurosci.* **21**, 156–158 (2018).
71. Zhang, K. et al. The C9orf72 repeat expansion disrupts nucleocytoplasmic transport. *Nature* **525**, 56–61 (2015).
72. Chou, C. C. et al. TDP-43 pathology disrupts nuclear pore complexes and nucleocytoplasmic transport in ALS/FTD. *Nat. Neurosci.* **21**, 228–239 (2018).

Methods

Cell lines, cell culture and transient transfections

HEK293T cells were obtained from Invitrogen (now Thermo Fisher), DNAJB6 KO HEK293T cells were generated using CRISPR–Cas9 KO strategies (for details, see below), U2OS cells were obtained from the Danish Cancer Society Research Center (gift from Dr C. Dinant), HeLa and HeLa 4TorKO cells were a gift from Christian Schlieker (Yale School of Medicine), BeWo cells originate from the University Medical Center Groningen (UMCG) paediatrics department. HEK293T, DNAJB6 CRISPR–Cas9 KO HEK293T, U2OS, HeLa and HeLa 4TorKO cells were cultured according to standard protocols in in DMEM (Gibco) supplemented with 10% FCS (Greiner Bio-One), and penicillin/streptomycin (Invitrogen). BeWo cells were grown in F12 (Gibco) plus 10% FCS (Greiner Bio-One) and penicillin/streptomycin (Invitrogen). For transient transfections, cells were grown to 70–80% confluence in a 37 °C incubator at 5% CO_2, in 35-mm-diameter dishes coated with 0.0001% poly-L-lysine (Sigma) and/or on coated coverslips for confocal microscopy analysis. For live cell imagining, cells were grown in 35-mm-diameter glass-bottom wells (MatTek). For siRNA, CRISPRi and complementary DNA plasmids, cells were transfected with Lipofectamine 2000 (Invitrogen) according to the manufacturer's instructions.

Used siRNAs, all from Dharmacon/Horizon: SMARTpool siGENOME non-targeting (D-001206-13-20), SMARTpool Accell DNAJB6 siRNA (E-013020-00-0005), SMARTpool siGENOME NUP98 (M-013078-01-0005), SMARTpool siGENOME NUP133 siRNA (M-013322-01-0005), Custom DNAJB6 duplex siRNA 5′UTR CAUUCCAACAAUCUCGUAAUU, Custom siRNA ELYS AAUAUCUACAUAAUUGCUCUU, Custom siRNA Nup153 GGACUUGUUAGAUCUAGUU.

Gene cloning and generation of mutants

Information about the (construction of) the V5-DNAJB6 WT is described in Hageman et al.[15] and Kakkar et al.[16]. GFP-DNAJB6b was made through PCR of GFP with HindIII and BamHI restriction sites to replace the V5-tag of V5-DNAJB6b. To make the BioID2-tagged DNAJB6b, DNAJB6b was amplified from the V5-DNAJB6b vector and digested with NotI and BamHI and inserted into myc-BioID2 pcDNA3.1 (74223; Addgene). siRNA resistant mutants of DNAJB6 were created by introducing five nucleotide polymorphisms at the siRNA binding site with site-directed mutagenesis (Agilent, 200523). Torsin A-GFP (32119) was obtained from Addgene and cloned into the mammalian expression pcDNA3.1 vector with restriction sites HindIII and BamHI. The ER localization signal was re-inserted using oligos. The Torsin A ΔE302 mutation was made by site-directed mutagenesis (Agilent, 200523). MLF2-GFP was created by PCR of MLF2 from cDNA extracted from HEK293T cells and inserted into the pEGFP vector. GFP-Nup153 (87340) was obtained from Addgene. GFP-Nup153FG (aa 875–1,475) was created by PCR of the FG domain of Nup153 and inserted into the pEGFP vector. The GFP-Nup153AG construct was kindly provided by Edward Lemke. For protein purification, the cDNA fragment encoding human Nup153FG (hNup153FG), and yeast Nup100 (yNup100FG, aa 1–580), and the full-length chaperones DNAJB6b and DNAJA1 were cloned in the expression plasmid pSF350, containing a His6-tag at the N-terminal end and a cysteine residue at the C-terminal end. The constructs expressing yeast Nup116 (yNup116FG, aa 1–725) and yeast Nup145N (yNup145NFG, aa 1–219) were kindly provided by Dirk Görlich.

CRISPRi

CRISPRi was performed following the protocol from Larson et al.[73]. Briefly, dCas9-KRAB (71237) and single guide RNA (sgRNA) containing an mCherry tag (44248) were obtained from Addgene. The dCas9-KRAB was cloned into the mammalian expression vector pcDNA3.1. The mCherry tag in the sgRNA vector was replaced by an mTurquoise to make full use of the colour spectrum for immunofluorescence. sgRNA was designed by CRISPR-ERA v1.2 (http://crispr-era.stanford.edu/) following the standard protocol. sgRNAs sequences for the Torsins are: Torsin A: CGGCGCGAGAACAAGCAGGG, Torsin B: CTTCGAGGAGCGGGATGTTG. HEK293T cells in six-well plates were transfected using Lipofectamine 2000 according to the manufacturer's protocols with 1 µg Cas9-KRAB plasmid and total of 1.5 µg sgRNA plasmid(s). Cells were fixed for either immunofluorescence or electron microscopy (EM).

BioID2 pulldown

BioID2-DNAJB6b transfected HEK293T cells were incubated for 24 h in complete medium supplemented with 50 µM biotin. After two ice-cold PBS washes, cells were scraped in 1 ml PBS and centrifuged for 5 min at 1,000 rpm at 4 °C. The PBS was removed and pellets were snap frozen in liquid nitrogen. After thawing on ice, cells were lysed in 250 µl lysis buffer (150 mM NaCl, 50 mM Tris pH 8.0, 0.2% NP-40, 0.2% SDS, 1× complete protease inhibitor EDTA free (Roche) and ~30 units Benzonase (EMD Millipore, 70746-4)), vortexed and put on ice. Lysates were vortexed every 10 min for 1 h to assure full lysis. Lysates were centrifuged for 10 min at 2,000*g* at 4 °C, supernatants were transferred to new tubes and pellets were discarded. Protein concentrations were equalized in washing buffer (150 mM NaCl, 50 mM Tris pH 8.0, 1 mM EDTA, 0.2% NP-40, 0.2% SDS and 1× complete protease inhibitor (Roche)) and 50 µl put in new tubes labelled 'input' with 25 µl of 4× Laemli buffer with 20% β-mercaptoethanol and immediately boiled for 5 min. To the rest of the samples 30 µl of pre-washed (2× in 500 µl washing buffer) magnetic streptavidin beads (Dynabeads MyOne Streptavidin, Invitrogen, 65001) were added and incubated on a roller in a 50 ml tube at 4 °C overnight. All subsequent steps were performed at room temperature. Supernatant was removed (50 µl was taken for the 'supernatant' fraction), and beads were washed twice in 500 µl washing buffer, twice in 500 µl high-salt buffer (500 mM NaCl, 50 mM Tris pH 8.0, 1 mM EDTA, 0.2% NP-40 and 0.2% SDS), and twice in 500 µl washing buffer. Then, 50 µl of 4× Laemli buffer with 20% β-mercaptoethanol was added and beads were incubated for 15 min at 70 °C. Sample was removed from beads and boiled for 5 min, labelled 'pulldown'. Then, 5 µl input and 10 µl pulldown were loaded for western blotting and probed with indicated antibodies.

Immunofluorescence

For immunofluorescence, cells were washed once with PBS to remove residual medium and fixed using 2% paraformaldehyde (PFA) in PBS for 15 min. After washing twice with PBS, cells were permeabilized with 0.1% Triton X-100 for 5 min at room temperature and washed again with PBS. Then the cells were washed twice in PBS+ (PBS complemented with 0.5% bovine serum albumin and 0.15% glycine) and incubated with 35 µl primary antibody in PBS+ at the indicated dilution, covered with parafilm and incubated at 4 °C overnight. The next day, cells were washed four times with PBS+ and incubated with the appropriate secondary antibodies conjugated to Alexa488/Alexa594 (Thermo Fisher Scientific) for 1.5–2 h at room temperature in PBS+. The nuclei were stained using Hoechst 33342 dye (Life Technologies) at 1:2,000 dilution in PBS for 5–10 min at room temperature. Finally, the cells were washed twice with PBS and mounted in 80% glycerol for imaging.

PLA

PLA was performed as previously described[74]. In short, cells were grown on poly-L-lysine-coated diagnostic slides with eight cavities and fixed using 4% PFA in PBS for 30 min. After washing twice with PBS, cells were permeabilized with 0.5% Triton X-100 for 10 min at room temperature and washed with TBST. A humid chamber was prepared by covering the bottom of a closed box with wet tissues. The diagnostic slide was placed in this chamber during the following incubation steps. Cells were blocked with Blocking Buffer for 30 min at 37 °C followed by incubation with 30 µl primary antibodies in Antibody Dilution Buffer (1:500) for 1 h at 37 °C (both Blocking Buffer and Antibody Dilution Buffer are provided with the Duolink In Situ PLA Probes (DUO92002 and DUO92004, Sigma-Aldrich)). Afterwards, cells were washed twice with Wash Buffer 'A' (10 mM Tris, 150 mM NaCl and 0.05% Tween-20,

pH 7.4) and incubated with the secondary antibodies anti-mouse MINUS and anti-rabbit PLUS (Duolink In Situ PLA Probe) for 1 h at 37 °C and washed twice with Wash Buffer 'A'. Then, cells were incubated with ligation mixture for 30 min at 37 °C and washed again twice with Wash Buffer 'A' before incubation with the amplification mixture for 100 min at 37 °C (all reagents are included in the Duolink In Situ Detection Reagents Orange (DUO92007, Sigma-Aldrich)). Finally, the cells were washed twice in Wash Buffer 'B' (200 mM Tris and 100 mM NaCl, pH 7.4), and once in 1:100 Wash Buffer 'B' in ultrapure water, before they were incubated with Hoechst for 5 min and mounted in 80% glycerol.

Image acquisition

Images were acquired with Leica SP8 confocal microscope, using LAS-AFX software. Cells were imaged with 63× and 20× objectives. Live cell imaging for FRAP was performed on a Carl Zeiss780 confocal microscope with an incubation chamber at 37 °C and 5% CO_2. The captured images were processed using Leica Software, Zeiss software, ICY, Fiji/ImageJ, CellProfiler and Adobe CC.

FRAP analysis

HEK293T cells were grown in 35 mm poly-D-lysine-coated glass-bottom dishes (MatTek) before live cell imaging on a Zeiss780 confocal microscope in an incubation chamber at 37 °C and 5% CO_2. A FRAP region of interest covering a part of an accumulation of GFP-Nup153FG was selected, and imaged for ten iterations before the FRAP region was bleached for one iteration at the highest intensity of the 488 nm 25 mW argon laser focused by a PlanApochromat 63×/1.40 oil differential interference contrast lens. Recovery of fluorescence was monitored at the shortest interval possible (millisecond range) at 0.5% of the laser intensity used for bleaching. For generation of FRAP curves, the intensity values were normalized to the average intensity of the ten pre-bleach iterations, and mean ± standard deviation (s.d.) was plotted.

Hexanediol treatment

Before fixing cells for immunofluorescence, the culture medium was removed and cells were washed once with PBS at 37 °C.Cells were then treated by adding new culture medium containing 5% 1,6-hexanediol or 2,5-haxanediol for 2 min.

5-Ethynyl uridine labelling

Twenty-four hours before fixation of the cells, cells were labelled using medium complemented with 20 µM 5-ethynyl uridine (Enzo Life Sciences, JBS-CLK-N002-10). After, the immunofluorescence protocol was followed, but before PBS+ washes, cells were incubated for 30 min with 100 µl (for six-well plate) label mix (2 mM $CuSO_4.5H_2O$, 8 µM Sulfo-Cy3 (or other CyColor)-Azide (Lumiprobe, A1330), 20 mg ml^{-1} ascorbic acid, in PBS), and washed twice with PBS.

Double thymidine block and FACS sorting for cell cycle analysis

Cells were grown to approximately 40% confluency when synchronized by adding culture medium containing 2 mM thymidine for 14 h. Then cells were washed twice with PBS followed by adding culture medium with 24 µM deoxycytidine for 9 h. The thymidine treatment was repeated for 14 h before changing to 24 µM deoxycytidine again, releasing the second block. Cells were collected by trypsin either immediately or at the indicated timepoints after release of the block. Trypsin was neutralized by adding culture medium. To determine with FACs the cell cycle phase (G1, S or G2/M) of the synchronized cells, cells were fixed in 70% ethanol overnight at 4 °C. DNA content was stained with 50 mg ml^{-1} propidium iodide and 1 mg ml^{-1} RNase A for 30 min at 37 °C in the dark before FACS analysis. Analysis was performed with FlowJo.

Antibodies

The following antibodies were used (in brackets company, ordering number and dilution, respectively). Mouse monoclonal antibodies: RanGap1 (Santa Cruz Biotechnology, sc-28322, 1:500), Nup50 (Santa Cruz Biotechnology, sc-398993, 1:250), Nup98 (Santa Cruz Biotechnology, sc-74553, 1:500), Nup153 (Santa Cruz Biotechnology, sc-101544, 1:150 and Biolegend, 906201 (QE5), 1:250), Nup205 (Santa Cruz Biotechnology, sc-377047, 1:250), RanBP2/Nup358 (Santa Cruz Biotechnology, sc-74518, 1:250), TPR (Santa Cruz Biotechnology, sc-271565, 1:200), mAb414 (Biolegend, 902901, 1:500), Lamin B1 (Santa Cruz Biotechnology, sc-365962, 1:500), HSP70 (Stressgen, SPA-810, 1:250), HSP70B' (HSPA6) (Enzo Life Sciences, ADI-SPA-754, 1:1,000), ubiquitin (Sigma-Aldrich, ST1200 (FK2), 1:1,000), GFP/YFP (Clontech, JL-8, 1:500), His (Qiagen, 34670, 1:5,000), GAPDH (Fitzgerald, 10R-G109A, 1:10,000) and IgGk BP-HRP (Santa Cruz Biotechnology, sc-516102, 1:250). Rabbit polyclonal antibodies: ELYS (Abcam, ab14431, 1:1,000) and DNAJB6 (Braakman lab Utrecht, 1:250). Goat polyclonal antibody: Nup133 (Santa Cruz Biotechnology, sc-27392, 1:100). Secondary antibodies: anti-mouse-IgG HRP (GE Healthcare, GENXA931, 1:5,000), anti-rabbit-IgG HRP (GE Healthcare, GENA934, 1:5,000), anti-goat-IgG HRP (Santa Cruz Biotechnology, sc-2020, 1:5,000), Alexa Fluor 488 donkey anti-rabbit IgG (H + L) (Thermo Fisher, A21202, 1:1,500), Alexa Fluor 594 donkey anti-mouse IgG (H + L) (Thermo Fisher, A21203, 1:1,500), Alexa Fluor 633 goat anti-rabbit IgG (H + L) (Thermo Fisher, A21070, 1:1,500) and Pierce High Sensitivity Streptavidin-HRP (Thermo Scientific, 21130, 1:1,500).

TEM

HEK293T DNAJB6 KO cells were fixed in an equal volume of 2% paraformaldehyde and 0.2% glutaraldehyde in 0.1 M sodium cacodylate buffer (pH 7.4) in medium and incubated for 10 min. Cells were then incubated with fresh pure fixative (2% PFA and 0.2% GA) for 30 min and rinsed twice with 0.1 M sodium cacodylate. All steps were performed at room temperature. Epon EM embedding was performed as described previously[75]. Large-scale EM datasets of HEK293T WT and HEK239T DNAJB6 KO cells are available at http://www.nanotomy.org/OA/Kuiper2022NCB/.

Immunoelectron microscopy

HEK293T cells with CRISPRi knockdown of Torsin A and Torsin B, with or without overexpression of GFP-DNAJB6b, were fixed by adding an equal volume of culture medium of freshly prepared double-strength fixative (4% formaldehyde and 0.4% glutaraldehyde in 0.1 M phosphate buffer, pH 7.4) for 5 minutes at room temperature. This mixture was then replaced by one volume of single-strength fixative (2% formaldehyde and 0.2% glutaraldehyde in 0.1 M phosphate buffer, pH 7.4) before incubating the cells for additional 3 h at room temperature. Cell embedding, ultrathin cryosectioning (50–60 nm) and immuno-gold labelling were performed as previously described[44]. Sections were immuno-labelled using either a rabbit anti-GFP (Abcam) or an anti-DNAJB6 antibodies, which were subsequently detected with protein A-gold (Cell Microscopy Center, UMC Utrecht, the Netherlands). The percentage of herniations positive for DNAJB6 or GFP-DNAJB6b was determined by analysis of about 135 herniations per condition. Co-localization of DNAJB6 or GFP-DNAJB6b with NPCs at the herniation was determined by analysis of double labelling for DNAJB6 or GFP and NPCs in over 110 herniations per condition. For electron tomography, additional fiducial markers (15 nm protein A colloidal gold, Cell Microscopy Center, UMC Utrecht, the Netherlands) were layered on top of the thick cryosections after the immuno-gold labelling. For 2D imaging, cell sections were analysed using an 80 kV transmission electron microscope CM100bio TEM (FEI).

Electron tomography: 3D reconstruction and modelling

Three-dimensional models of GFP-DNAJB6b-positive and endogenous DNAJB6-positive herniations were obtained by electron tomography of 300- to 400-nm-thick cryosections. The areas of interest were selected on the basis of the immuno-gold detection of GFP-DNAJB6b, using a conventional 80 kV electron microscope, previous recording of the

double-tilt series with high voltage (200 kV) electron microscope. The tilt series images, recorded using a Tecnai T20 (FEI), were aligned using at least 20 fiducial gold particles, using the IMOD program package (University of Colorado, USA). The IMOD software was also used to create double tilt tomograms by combining two R-weighted back projection and/or SIRT tomograms. Filtering options in the IMOD package (median algorithm) were used to 'smooth' the tomograms. The tomograms had a final lateral resolution of approximately 4 nm based on the Crowther criterion. Double tilt tomograms were analysed and modelled also using the IMOD software. Features of interest were contoured manually in serial optical slices extracted from the tomogram, and used to create surface-rendered models.

Western blot analysis

Indicated sample amounts and 5 µl PageRuler Prestained Protein Ladder (Thermo Scientific) were loaded on 10% or 12% SDS–PAGE gels. SDS–PAGE was performed using the Bio-Rad Mini-PROTEAN 3 system. After SDS–PAGE, proteins were transferred to nitrocellulose membranes by semiwet electrotransfer with the Bio-Rad Trans-Blot Turbo transfer system. To prevent non-specific protein binding, membranes were incubated in 5% (w/v) non-fat dried milk in PBS-Tween (PBS-T) for 1 h at room temperature. Membranes were washed in PBS-T and incubated at 4 °C overnight with indicated antibodies. Membranes were washed three times for 10 min and incubated for at least 1 h in HRP-conjugated secondary antibodies (GE Healthcare) at 1:8,000 dilution in PBS-T. After incubation, membranes were washed three times for 10 min in PBS-T and enhanced chemiluminescence detection was performed using the ECL Western Blotting substrate kit (Thermo Scientific). Quantifications were performed using Bio-Rad imaging software, and graphs were generated using GraphPad Prism. Statistical significance was analysed using an independent Student's *t*-test. $P < 0.05$ was considered statistically significant. Values are expressed as mean ± standard error of the mean (s.e.m.).

Protein extraction for FTA

Forty-eight hours after transfection, cells were washed once in cold PBS and scraped in 200 µl lysis buffer (25 mM HEPES, 100 mM NaCl, 1 mM $MgCl_2$, 1% NP-40 (Igepal CA-630, Sigma), EDTA-free complete protease inhibitors cocktail (Roche) and Benzonase (EMD Millipore) (~90 units ml^{-1})), and left on ice for minimum of 30 min with intermittent vortexing until chromatin was dissolved. Protein concentrations were determined using DC protein assay (Bio-Rad). Concentrations were equalized and diluted in filter trap assay (FTA) buffer (10 mM Tris–HCl pH 8.0, 150 mM NaCl and 50 mM dithiothreitol, 0.5% SDS), boiled for 5 min and prepared in three five-fold serial dilutions into a final of 1×, 5× and 25× diluted samples for FTA. FTA samples were loaded onto a 0.2-µm-pore-size cellulose acetate membrane pre-washed with 0.1% SDS-containing FTA buffer. Membranes were washed two times with 0.1% SDS-containing FTA buffer, blocked with 5% non-fat milk and blotted with anti-GFP/YFP (Clontech). After HRP-conjugated secondary antibody incubation, visualization was performed using enhanced chemiluminescence and ChemiDoc Imaging System (Bio-Rad). Bands were measured (ImageLab 5.2.1), and the measurement of the three dilutions was averaged. Values normalized to control were plotted in a graph.

Gene cloning and generation of mutants

For protein purification, the cDNA fragment encoding human Nup153FG (hNup153FG, aa 875–1,475), and yeast Nup100 (yNup100FG, aa 1–580), and the full-length chaperones DNAJB6b, DNAJB2a, DNAJB8, DNAJB1, DNAJA1 and DNAJB6b mutants (H31Q, 18× S/T > A, 12× F > A, Δ79–115 (exon 5)), were cloned in the expression plasmid pSF350, containing a His10-tag at the N-terminal end and a cysteine residue at the C-terminal end. The constructs expressing yeast Nup116 (yNup116FG, aa 1–725) and yeast Nup145N (yNup145NFG, aa 1–219) were kindly provided by Dirk Görlich.

Protein purification

The expression of FG-Nup fragments, DNAJB6b, DNAJA1, MBP-mCherry and DNAJB6b mutants (18× S/T > A, 12× F > A, Δ79–115 (exon 5)), was performed in 200 ml cell cultures of *E. coli* cells (OD_{600} = 0.5–0.8, grown at 37 °C) by adding 0.5 mM isopropyl-β-D-thiogalactoside (#10724815001) for 5 h at 20 °C. Cells were collected by centrifugation (4,500*g*, 15 min, 4 °C), and pellets were stored at −80 °C. For the purification of FG fragments and the chaperones DNAJB6, DNAJA1 and DNAJB6b mutants (18× S/T-A, 12× F-A, Δ79–119 (exon 5)), the cell pellets were resuspended in 10 ml lysis buffer (100 mM Tris–HCl and 2 M guanidine–HCl buffer, pH 8.0) (Thermo Scientific, #24110), supplemented with protease inhibitor cocktail (cOmplete ULTRA Tablets, Mini, EDTA-free, EASYpack Protease Inhibitor Cocktail, #5892791001), 1 mM phenylmethylsulfonyl fluoride (Serva, #32395.02) and 5 mM DL-1,4-dithiothreitol (DTT; 99%, ACROS Organics, #10215550) and disrupted with glass beads (disruptor beads 0.1 mm, Scientific Industries, SI-BG01) in the Fastprep. Lysed cells were clarified by centrifugation for 5 min at 20,000*g*, and the supernatant was centrifuged again for 15 min at 20,000*g*. The supernatant was equilibrated in lysis buffer and incubated with Ni-sepharose beads (Ni Sepharose 6Fast Flow, Cytiva, 17-5318-03) at 4 °C for 1 h. Beads were washed two times with 10 ml of lysis buffer (100 mM Tris–HCl and 2 M guanidine–HCl, pH 8.0) supplemented with 50 mM imidazole (PUFFERAN ≥99%, CarlRoth, X998.4) and 2.5 mM DTT, using Poly-Prep columns (Poly-Prep Chromatography Columns, Bio-Rad, #7311550). Proteins were eluted with 500 mM imidazole (100 mM Tris–HCl 2 M, guanidine–HCl, pH 8.0, and 10% glycerol).

Expression and purification of MBP-mCherry was performed essentially as described above, but using 50 mM Tris–HCl 150 mM NaCl, pH 8.0 buffer for cell lysis and protein purification. For FG-Nup fragments and DNAJB6b labelling, the proteins were purified essentially as described above, but for the second wash 10 ml of lysis buffer (100 mM Tris–HCl and 2 M guanidine–HCl, pH 8.0) supplemented with 50 mM imidazole (PUFFERAN ≥99 %, CarlRoth, X998.4) was used to wash away residual DTT. After Ni-sepharose beads purification, proteins were incubated for 1 h at room temperature with 4.5 µg of either fluorescein-5-maleimide (Thermo-Scientific, 62245) for the FG-Nups or Texas red-maleimide (Texas Red C2 Maleimide, Thermo-Scientific, T6008) for DNAJB6b, followed by another wash in lysis buffer. Proteins were eluted with 500 mM imidazole (100 mM Tris–HCl, 2 M guanidine–HCl, pH 8.0, and 10% glycerol).

The expression of GFP-tagged IDPs 1 and 2 (IDP1 is the disordered region of yHeh2 protein (h2NLS-L)[55]; IDP2 is a synthetic IDP (h2NLS-LP50)[56]); was performed in *Lactococcus lactis* cells. Cell disruption was performed by cryomilling (Retch). IDP1 and IDP2 were purified essentially as described above, using 100 mM Tris–HCl 2 M guanidine–HCl buffer, pH 8.0 for cell lysis and protein purification.

A 5 µl fraction of the purified proteins was checked on SDS–PAGE electrophoresis (Extended Data Fig. 10a). Cysteine residues of purified proteins were reduced with 10 mM DTT for 30 min at 50 °C and blocked with 15 mM iodoacetimide alkylating reagent (Sigma Aldrich, #I1149-25G) for 30 min at room temperature to prevent the formation of disulfide bonds. Proteins were concentrated using Vivaspin Protein Concentrator spin columns (Vivaspin 2, 10/30 kDa MWCO Polyethersulfone, Cytiva, 28-9322-47, 28-9322-48), according to the manufacturer's instructions.

Measurement of final protein concentration was performed using BCA protein assay (Pierce BCA Protein Assay Kit, Thermo Scientific, #23227), according to the manufacturer's instructions, using BSA (Pierce Bovine Serum Albumin Standard Ampules, 2 mg ml^{-1}, #23209) as a standard.

Circular dichroism spectroscopy

Purified proteins were diluted to a concentration of either 0.2 µM (DNAJB6 WT), 0.67 µM (18× S/T > A mutant) or 15 µM (12× F > A and Δ79–115 mutant) in the assay buffer (50 mM Tris–HCl and 150 mM

NaCl, pH 8.0). Ultraviolet–visible absorption and electronic circular dichroism (eCD) spectra were recorded between 500 nm and 200 nm in a quartz (QS) cuvette with either a 2 mm (12× F > A mutant and Δ79–115 mutant) or 5 cm (DNAJB6 WT and 18× S/T > A mutant) path length using a AnalyticJena Specord 210 and a Jasco J-815 CD spectrometer, respectively (Extended Data Fig. 10b). The absorbance in the range of interest was kept below a maximum of 1.5. For eCD, the scanning rate was 100 nm min^{-1}, the digital integration time per data point (DIT) was 2 s and the sensitivity was set to standard. The data were cropped at the wavelength where the high tension exceeded 600 V. Data were processed by subtracting the background signal from the buffer, and data units (mdeg) were converted to molar ellipticity.

FTA of purified proteins

To assay the effect of crowding agents in the aggregation/phase transition of FG-Nups, purified proteins were diluted at the indicated concentrations in the assay buffer (50 mM Tris–HCl and 150 mM NaCl, pH 8.0), containing varying concentrations of the corresponding crowding agent: 0/5/10/15% w/v of serine (L-serine, 99%, ACROS Organics, AC132660250), 0/5/10/15% w/v of polyethylene glycol 3350 (PEG; Sigma-Aldrich, P4338-2KG) and 0/5/10/15% w/v of Ficoll (Sigma-Aldrich, F2637-25G). To assay the effect of the chaperone DNAJB6b in the aggregation/phase transition of FG-Nup fragments, purified FG fragments were mixed with purified DNAJB6b, or the corresponding control protein (BSA, MBP-mCherry, DNAJA1, IDP1 or IDP2), in the assay buffer (50 mM Tris–HCl and 150 mM NaCl, pH 8.0) containing 10% PEG. In addition, three mutational variants of DNAJB6b were tested for their ability to supress FG-Nup aggregation (18× S/T > A, 12× F > A and Δ79–115 (exon 5) mutant). Aggregation assays were performed with a protein concentration of 3 µM or 6 µM in a final volume of 20 µl, at 25 °C for either 1 h or 3 h. While for hNup153FG and yNup100FG 1 h was sufficient to form SDS-insoluble aggregates in assay buffer, yNup116FG required 3 h to form aggregates. For yNup145N, the buffer composition was adjusted to 50 mM NaCl, 100 mM sodium phosphate, pH 6, containing 10% PEG3350 (w/v) to allow for the formation of SDS-insoluble aggregates (at 25 °C for 1 h).

For FTA, three trans-blot papers (Bio-Dot SF Filter Paper, Bio-Rad, #1620161) and one cellulose acetate membrane (cellulose acetate membrane filters, 0.2 µm, Sterlitech, CA023001) were soaked in either 150 mM NaCl, 50 mM Tris–HCl pH 8.0 (hNup153FG, yNup100FG and yNup116FG) or 50 mM NaCl, 100 mM sodium phosphate pH 8.0 (yNup145N FG) buffer, placed on the Bio-Dot apparatus (Bio-Rad, #1703938), and washed four times with sample buffer (150 mM NaCl and 50 mM Tris–HCl, pH 8.0/50 mM NaCl and 100 mM sodium phosphate pH 8.0), applying constant vacuum. Samples were added to 180 µl of sample buffer supplemented with 0.5% SDS and mixed by vortex before loading in the Bio-Dot apparatus (Bio-Rad). After loading samples and applying constant vacuum, slots were washed twice with sample buffer (50 mM Tris–HCl and 150 mM NaCl, pH 8.0/50 mM NaCl and 100 mM sodium phosphate pH 8.0) and twice with wash buffer (150 mM NaCl and 50 mM Tris–HCl pH 8.0/50 mM NaCl and 100 mM sodium phosphate pH 8.0 supplemented with 0.1% SDS). After blocking for 1 h in 2.5% BSA (Acros Organics 268131000, #10450141) in PBS with 0.1% Tween-20 (MP Biomedicals, MP1TWEEN201), the membrane was incubated with mouse primary antibody anti-His (1:5,000, monoclonal mouse Tetra-His antibody, Qiagen, #34670) in 2.5% BSA in PBS-T overnight at 4 °C, washed three times with PBS-T, incubated with anti-mouse secondary antibody m-IgGk BP-HRP (1:5,000, Santa Cruz Biotechnology, sc-516102) in 2.5% BSA in PBS-T for 1 h at room temperature, and washed three times with PBS-T. Chemiluminescence was detected using ECL substrate (GE Healthcare, RPN2232) according to the manufacturer's instructions on a ChemiDoc Touch Imaging System (Bio-Rad).

Sedimentation assays

DNAJB6b, isolated as described above, was diluted to 3 µM in TBS and incubated at room temperature for 30 min. yNup100FG protein, isolated as described above, was diluted to 60 µM in 2 M Gu–HCl, 100 mM Tris–HCl pH 8. For each sedimentation assay 1 µl yNup100FG was pipetted in a low-protein-binding tube and subsequently 10 µl DNAJB6b (or TBS for the control condition), and 10 µl of 20% PEG in TBS was added, and the mixture was shortly vortexed. The samples were incubated for 0, 30, 90 or 270 min at room temperature, after which 5 µl of TBS was added to the samples and they were incubated for an additional 10 min. The soluble and insoluble fractions were then separated by centrifugation (17,900*g* for 10 min at room temperature). To determine the 1,6-hexanediol soluble fraction of the yNup100FG condensates, just before the centrifugation step, 5 µl 50% 1,6-hexanediol in TBS was added to the samples and incubated for 10 min at room temperature. Soluble fractions were analysed on SDS–PAGE. As a total protein control, a non-centrifuged 3 µM yNup100FG sample, in the presence or absence of 1.5 µM DNAJB6b, was loaded on the same gels. Band intensities from the Coomassie-stained gels were determined with the Bio-Rad Image Lab software, and calculated as relative intensity compared with total protein control band.

Fluorescence microscopy of purified proteins

Microscopy was performed on a DeltaVision Deconvolution Microscope (Applied Precision (GE)), using InsightSSITM Solid State Illumination, an Olympus UPLS Apo 100× oil-immersion objective (1.4 NA) and a CoolSNAP HQ2 camera. Excitation and emission were measured with the filter sets FITC 525/48 and A594 625/45. Imaging was performed in a temperature-controlled environment at 30 °C. hNup153FG and yNup100FG fragments labelled with fluorescein-5-maleimide were diluted out in the assay buffer (150 mM NaCl and 50 mM Tris–HCl, pH 8) containing 10% PEG3350 (w/v) at 25 °C for 1 h, in either the absence or the presence of DNAJB6b, either unlabelled or labelled with Texas red-maleimide, all at a 3 µM concentration (molar ratio 1:1). Fluorescence images were acquired with 30 *Z*-slices of 0.2 µm, and reference images were acquired at the middle of the sample using polarized light. Images were deconvolved using softWoRx software (GE Healthcare) and processed using open-source software Fiji/ImageJ to generate maximum *Z*-projections.

Statistics and reproducibility

Statistical testing was performed using GraphPad Prism software. The statistical tests that were used are indicated in the legends, and *P* values are indicated for all experiments. No statistical method was used to pre-determine sample size. No data were excluded from the analyses. The experiments were not randomized. The investigators were not blinded to allocation during experiments and outcome assessment. All repetitions (*n*) originate from independent experiments. EM data and quantification of these were based on large-scale (nanotomy) recordings. For the percentage of GFP- or DNAJB6-positive herniations, $n = 135$ herniations per condition were counted, and for double labelling, 110 herniations were counted. Findings in the IF data that were not quantified were observed in at least three independent experiments.

Reporting summary

Further information on research design is available in the Nature Research Reporting Summary linked to this article.

Data availability

Large-scale EM data are available via nanotomy.org (http://www.nanotomy.org/OA/Kuiper2022NCB/). All other data supporting the findings of this study are available from the corresponding author on reasonable request. Source data are provided with this paper.

References

73. Larson, M. H. et al. CRISPR interference (CRISPRi) for sequence-specific control of gene expression. *Nat. Protoc.* **8**, 2180–2196 (2013).

74. Alberts, N., Mathangasinghe, Y. & Nillegoda, N. B. In situ monitoring of transiently formed molecular chaperone assemblies in bacteria, yeast, and human cells. *J. Vis. Exp.* **151**, https://doi.org/10.3791/60172 (2019).
75. Kuipers, J., Kalicharan, R. D., Wolters, A. H. G., van Ham, T. J. & Giepmans, B. N. G. Large-scale scanning transmission electron microscopy (nanotomy) of healthy and injured zebrafish brain. *J. Vis. Exp.* **111**, 12–14 (2016).

Acknowledgements

E.F.E.K. is supported by a topmaster fellowship from the Groningen University Institute for Drug Exploration (GUIDE). H.H.K. and S.B. are supported by a grant from the CTH (grant no. 686728). L.M.V., H.H.K., S.B., M.K.M., P.G., T.B. and A.S. are supported by an NWO Groot (grant no. 685709). L.M.V., P.G., T.B. and A.S. are supported by a Vici grant (VI.C.192.031). M.M. is supported by an ALW Open Programme (ALWOP.355). We thank J. Brunsting and A. Blaauwbroek for practical assistance. We thank E. Lemke for providing us with the GFP-Nup153AG construct, D. Görlich for the yNup116FG and yNup145NFG constructs, and C. Schlieker for the HeLa 4TorKO cell line. We thank S. Cascarina for assistance with the LCD-Composer. We thank W. Browne for his help with the Circular dichroism measurements. Fluorescence and live cell imaging was performed in the UMCG Microscopy and Imaging Center (UMIC), sponsored by ZonMW grant 91111.006 and NWO 175-010-2009-023. EM 2D imaging was performed at the UMIC. Tomography imaging was performed at the EM facility of the Faculty of Science and Engineering of Groningen, the Netherlands.

Author contributions

E.F.E.K., H.H.K., L.M.V. and S.B. conceived the project. The experiments in Figs. 1, 2 and 4 were designed, performed and analysed by E.F.E.K., the TEM in Fig. 1f by J.K., the EM and tomography in Fig. 3 by M.M., the in vitro data in Figs. 5 and 6 by P.G., T.B. and A.S., and the PLA and DNAJB6b mutant experiments in Figs. 4b and 6c by M.K.M. Supervision was done by H.H.K., L.M.V., A.S., B.N.G.G. and S.B. The manuscript was written by E.F.E.K., S.B. and L.M.V., with input from all authors.

Competing interests

The authors declare no competing interests.

Additional information

Extended data is available for this paper at https://doi.org/10.1038/s41556-022-01010-x.

Supplementary information The online version contains supplementary material available at https://doi.org/10.1038/s41556-022-01010-x.

Correspondence and requests for materials should be addressed to E. F. Elsiena Kuiper, Harm H. Kampinga, Liesbeth M. Veenhoff or Steven Bergink.

Peer review information *Nature Cell Biology* thanks Janine Kirstein, and the other, anonymous reviewer(s) for their contribution to the peer review of this work. Peer reviewer reports are available.

https://doi.org/10.1038/s41556-022-01010-x

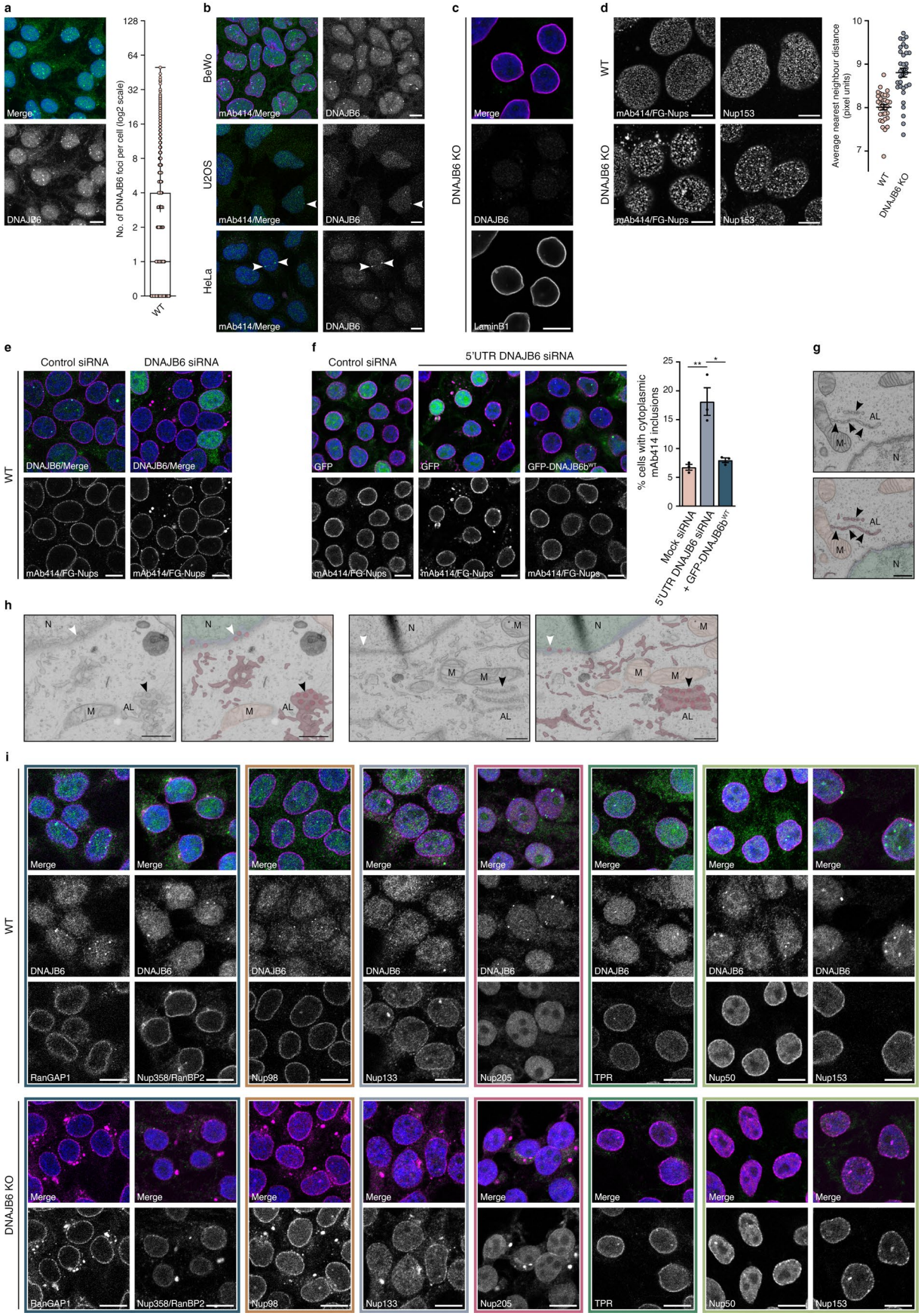

Extended Data Fig. 1 | See next page for caption.

https://doi.org/10.1038/s41556-022-01010-x

Extended Data Fig. 1 | Disruption of DNAJB6 expression leads to accumulation of annulate lamellae. a, DNAJB6 in HEK293T cells localizes to the cytoplasm and nucleus, and in foci at the nuclear rim. A Z-projection is shown. Graph depicts a quantification of the distribution of the number of DNAJB6 foci per cell. n = 3 independent experiments with 1272 cells analyzed; Log2 graph box and whiskers minimum to maximum with all data points; median indicated with a line and mean with a+. **b**, Different cell lines (BeWo, U2OS and HeLA) stained for DNAJB6 (green) and FG-Nups (mAb414, magenta). **c**, HEK293T DNAJB6 KO cells stained for DNAJB6 (green) and Lamin B1 (magenta). **d**, Images of mAb414 or Nup153-stained nuclear pores (focused on the top of the nucleus) in HEK293T and HEK293T DNAJB6 KO cells. Quantification of average nearest neighbour distance (in pixels) shows larger distances between NPCs in DNAJB6 KO cells. Every point represents one cell; WT n = 32 individual cells, DNAJB6 KO n = 33 individual cells; mean ± SEM. **e**, siRNA-mediated knockdown of DNAJB6 (green) (72 h) induces cytoplasmic accumulations of NPCs stained by mAb414 (magenta). **f**, HEK293T cells transfected with siRNA against the 5'UTR of DNAJB6 show accumulations of NPCs and by simultaneous expression of GFP-DNAJB6b^{WT} formation of these can be prevented. With a quantification of mAb414-positive accumulations after knockdown of DNAJB6. n = 3 independent experiments; unpaired t-test, 2-tailed p-value; *p = 0.0139, **p = 0.0097; mean ± SEM. **g**, In DNAJB6 KO cells, NPCs in the cytoplasm (annulate lamellae) visualized by transmission electron microscopy and pseudo-colored in bright pink, can be distinguished in cytoplasmic strings. Arrows point at individually identifiable NPCs. Nucleus indicated with N, mitochondrion indicated with M. Scale bar represents 500 nm. **h**, As in g, but now the white arrow head points at individually identifiable NPCs in the NE and black arrow heads at NPCs in the annulate lamellae. **i**, Individual channels of Fig. 1h. RanGap1, and different nucleoporins of the NPC Nup358, Nup133, Nup205, Nup98, TPR, Nup50, and Nup153 are stained (magenta) together with DNAJB6 (green) in WT and DNAJB6 KO cells. Source numerical data are available in source data.

https://doi.org/10.1038/s41556-022-01010-x

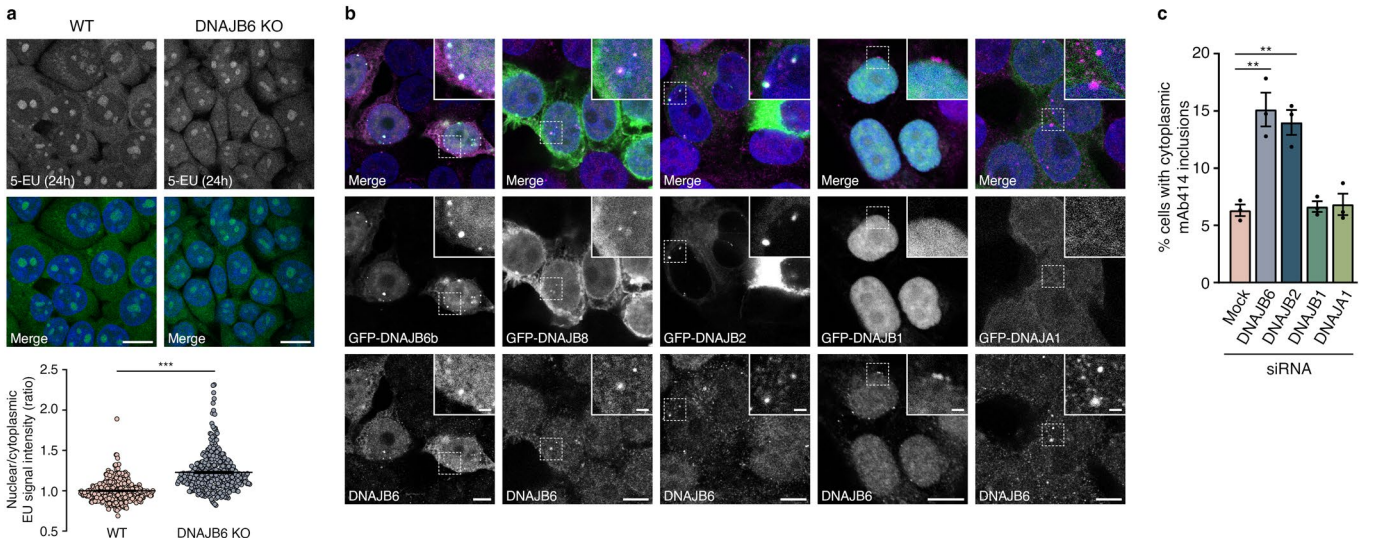

Extended Data Fig. 2 | Closely related JDPs of DNAJB6 also accumulate in foci and deletion can induce annulate lamellae. a, Representative images of HEK293T and HEK293T DNAJB6 KO cells cultured in medium containing the uridine analog 5-ethynyluridine (5-EU). 5-EU incorporation into newly transcribed RNA was detected by Cy3-azide (green). The ratio of nuclear to cytoplasmic signal intensities of RNA relative to HEK293T WT cells. Each individual point represents a single cell; WT n = 3 independent experiments with 327 cells examined, DNAJB6 KO n = 3 independent experiments with 323 cells examined; unpaired t-test, 2-tailed p-value; ***p < 0.0001; mean ± SEM. **b**, Colocalization of GFP-tagged DNAJB6b, DNAJB8, and DNAJB2 with endogenous DNAJB6. DNAJB1 and DNAJA1 do not colocalize with DNAJB6 foci at the NE. **c**, annulate lamellae formation under siRNA-mediated knockdown of DNAJB6, DNAJB2, DNAJB1, and DNAJA1. Knockdown of DNAJB6 and DNAJB2 leads to significant increase in annulate lamellae formation. All experiments n = 3 independent experiments with cells examined: control 4392, DNAJB6b 5073, DNAJB2 4118, DNAJB1 4059, DNAJA1 4184; unpaired t-test, 2-tailed p-value; **p = 0.0048 mock vs DNAJB6b, **p = 0.003 mock vs DNAJB2; mean ± SEM. Scale bars on all fluorescent images represent 10 µm, and on magnifications 2 µm. Source numerical data are available in source data.

https://doi.org/10.1038/s41556-022-01010-x

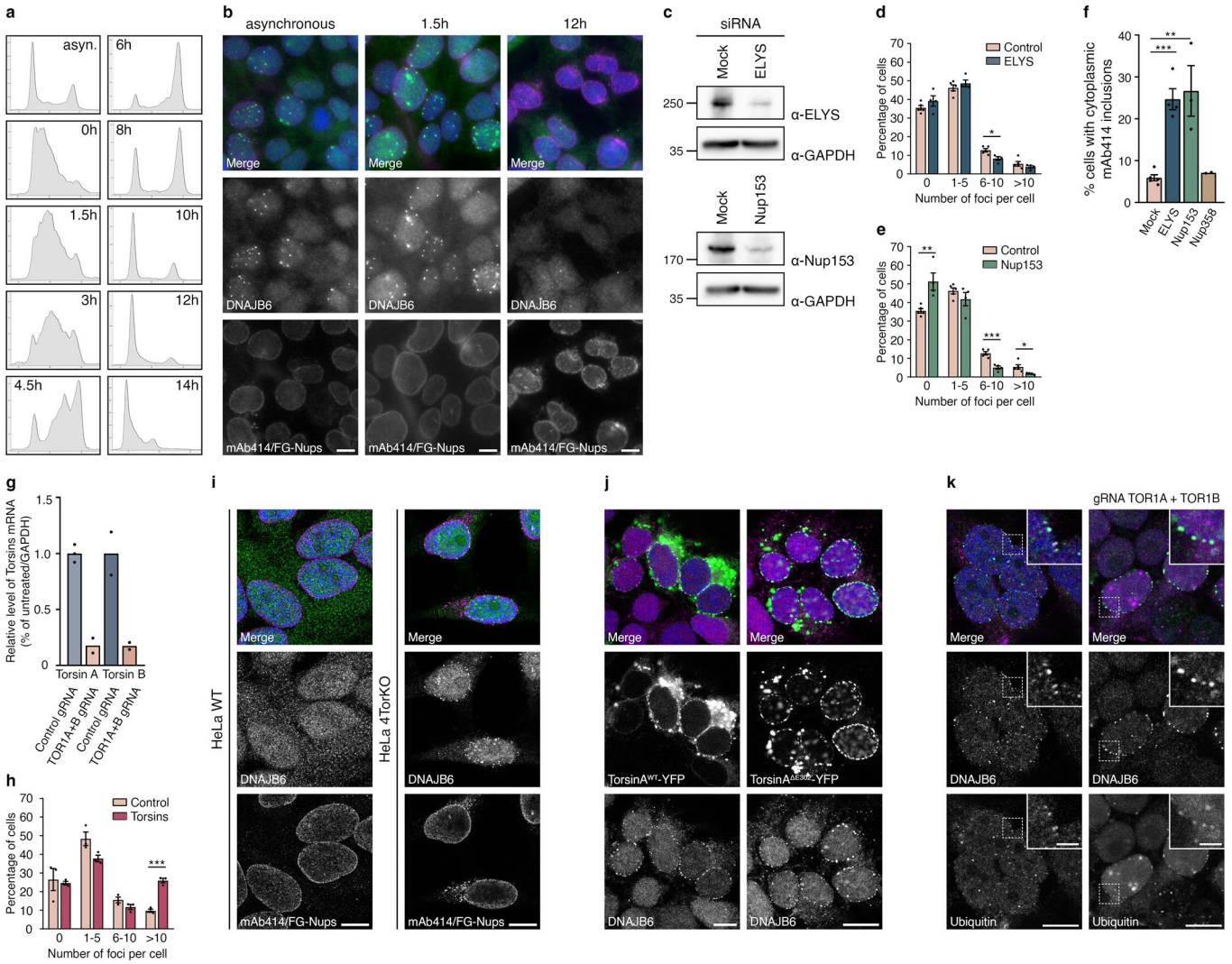

Extended Data Fig. 3 | DNAJB6 foci formation is cell cycle dependent and is related to interphase NPC assembly. a, Cell cycle progression profiles as analyzed by fluorescence-activated cell sorting (FACS). Cells were stained with propidium iodide to detect DNA content. **b**, DNAJB6 foci in HEK293T cells in asynchronized cells, and cells 1.5 h and 12 h after release from a double thymidine cell cycle synchronization. **c**, siRNA-mediated knockdown of ELYS and Nup153 in HEK293T cells visualized on SDS-PAGE with specific antibodies. **d**, **e**, Bar graphs of the data in Fig. 2b depicting a distribution of the amount of DNAJB6 foci per cell for the indicated siRNA treatment. NB: these conditions share the same control. **d**, *p = 0.0129, **e**, *p = 0.0304, **p = 0.0080, ***p = 0.0006; Control n = 5 independent experiments with 8298 cells examined, ELYS n = 4 independent experiments with 6839 cells examined, Nup153 n = 4 independent experiments with 7690 cells examined, automated with ICY; mean ± SEM. **f**, Quantification of percentage of cells with cytoplasmic NPC accumulations (AL) stained with mAb414 under siRNA knockdown of ELYS, Nup153, or Nup358. Control n = 5 independent experiments with 7317 cells examined, ELYS n = 4 independent experiments with 6323 cells examined, Nup153 n = 3 independent experiments with 4798 cells examined, Nup358 n = 2 independent experiments with 2264 cells examined; unpaired t-test, 2-tailed p-value; **p = 0.0037, ***p < 0.0001; mean ± SEM. **g**, qPCR on mRNA levels of Torsin A and B under control or knockdown conditions, normalized to GAPDH. Tor1A control n = 3 independent experiments, Tor1A, Tor1B control, and Tor1B n = 2 independent experiments. **h**, Bar graph of the data in Fig. 2c, depicting a distribution of the amount of DNAJB6 foci per cell. Control n = 3 independent experiments with 1272 cells examined, gRNA TOR1A + TOR1B n = 3 independent experiments with 952 cells examined, automated with ICY; mean is indicated with a cross; unpaired t-test, 2-tailed p-value; only significant differences are indicated; ***p = 0.0005; mean ± SEM. **i**, HeLa WT and HeLa 4TorKO cells stained for DNAJB6 (green) and FG-Nups with mAb414 (magenta). **j**, Overexpression of either TorsinA-GFP wildtype or ΔE302 (green) leads to an increase in foci at the nuclear envelope, containing DNAJB6 (magenta). **k**, Ubiquitin (magenta) colocalizes with DNAJB6 (green) at foci at the nuclear envelope and are increased upon Torsin knockdown (gRNA vector containing mTurquoise2 in the blue channel). Scale bars on all fluorescent images represent 10 µm, and on magnifications 2 µm. Source numerical data are available in source data.

https://doi.org/10.1038/s41556-022-01010-x

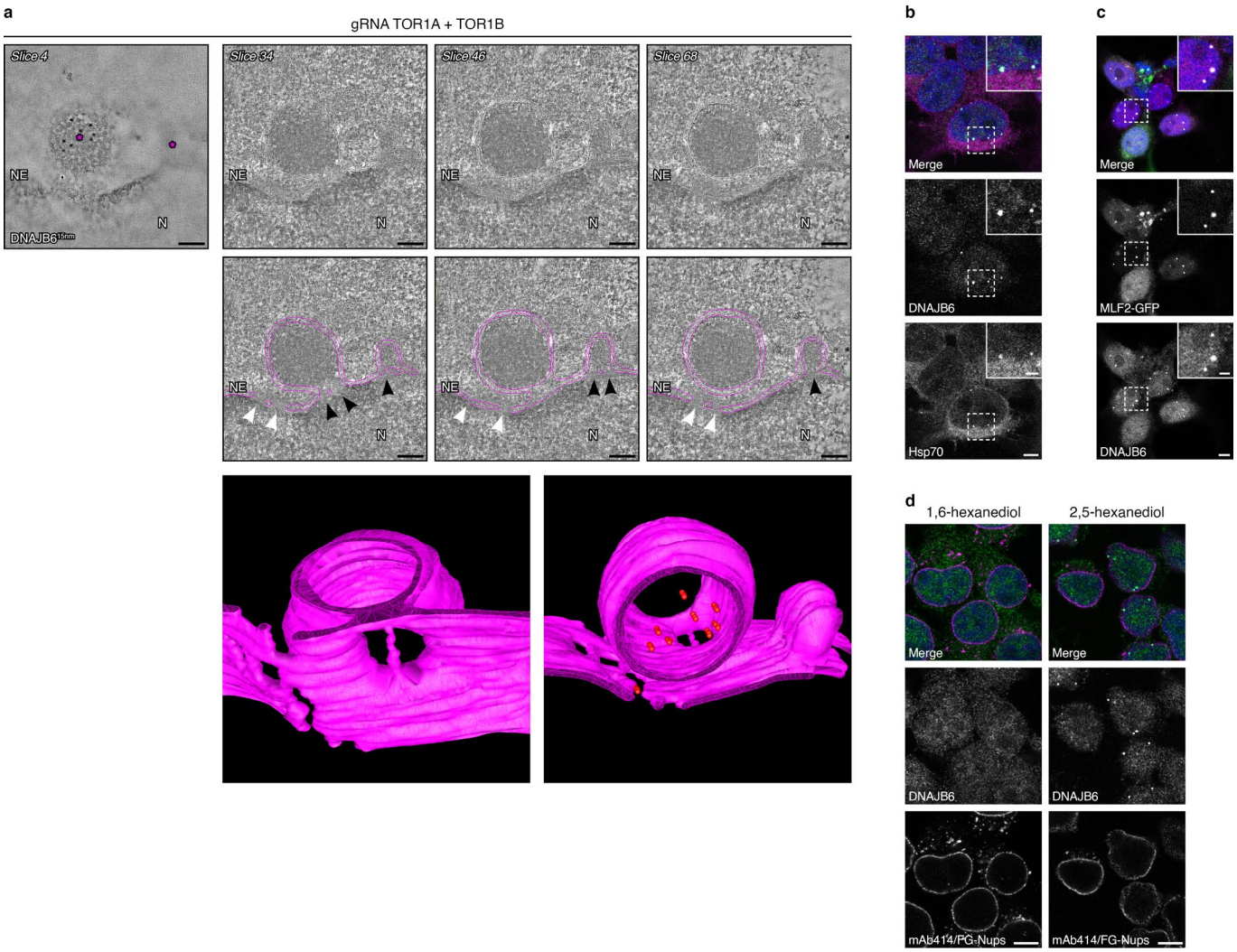

Extended Data Fig. 4 | DNAJB6 localizes to herniations at the NE and is dependent on intact NPCs. a, For immunoelectron tomography, surface labelling was used to select areas of interest prior to recording tilt series. Tomographic slice (Z slice 4) revealing the specific immunogold (15 nm) labelling on the surface of the cryosection. Asterisk indicating herniations. Indicated tomographic slices extracted from the tomogram showing herniations at the NE. In the bottom images, nuclear membranes are traced (pink). More electron dense areas can be observed at the neck of the herniations where the NE bends into the herniation, indicated by black arrow heads. NPCs are indicated with white arrow heads. Nucleus is indicated with N and nuclear envelope with NE. Scale bars represent 232 nm. Lower images are from the three-dimensional model (see Supplementary Video 2) of DNAJB6-positive herniations, obtained by electron tomography of 400 to 450 nm thick cryosections. The NE is represented in pink. Left is a view from the nuclear side showing the openings of the NPCs and of the herniations. Right shows the herniations with the localization of the DNAJB6 gold labelling in red. **b**, HSP70 (magenta) colocalizes with DNAJB6 (green) in foci at the NE. **c**, MLF2-GFP colocalizes with DNAJB6 (magenta) in foci at the NE. **d**, WT HEK293T cells treated with 5% 1,6-hexanediol for 2 minutes lose almost all DNAJB6 foci (green), while cells treated with 2,5-hexanediol have only a slight reduction in foci. Scale bars on all fluorescent images represent 5 µm, and on magnifications 2 µm.

https://doi.org/10.1038/s41556-022-01010-x

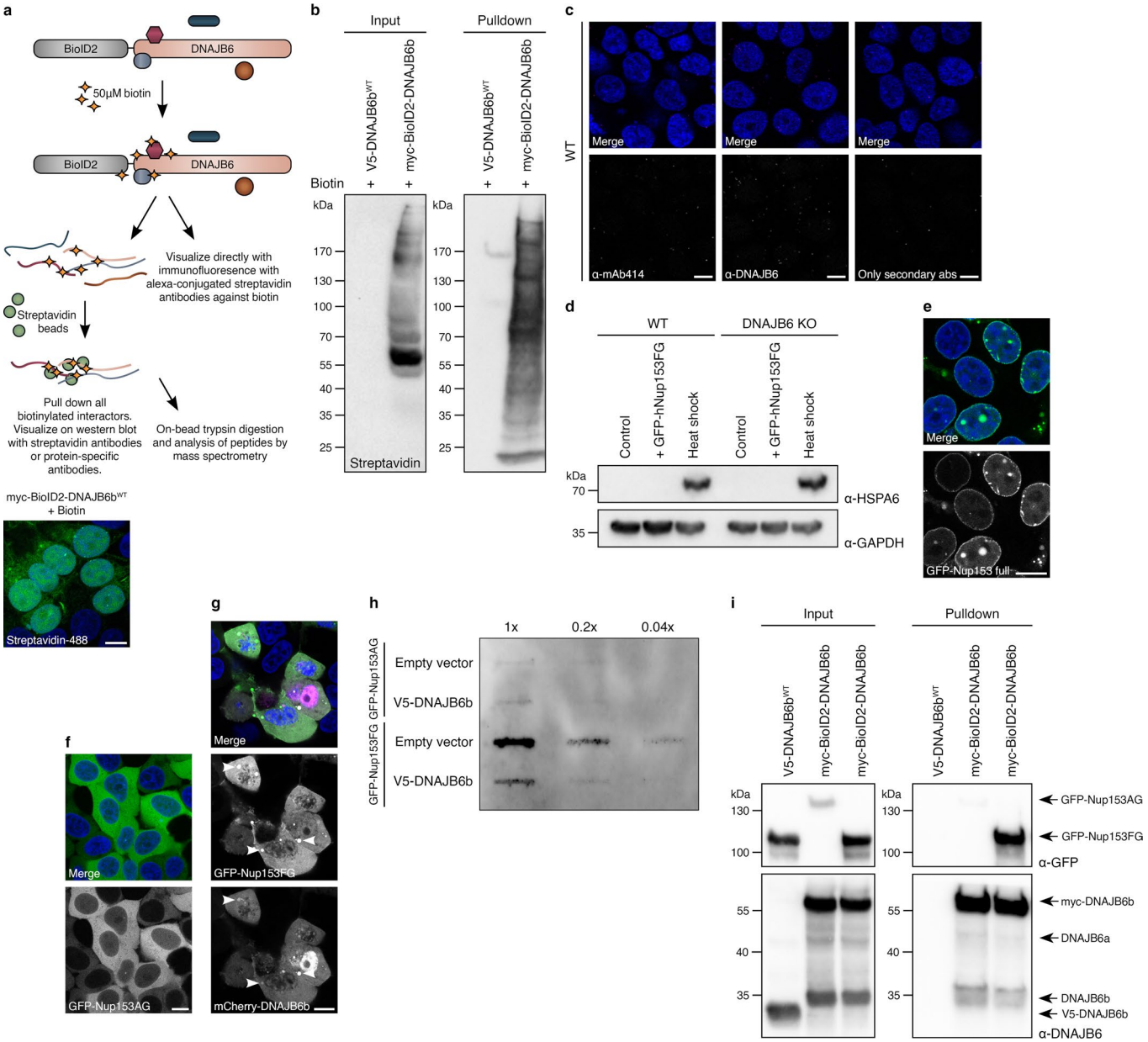

Extended Data Fig. 5 | The interaction of DNAJB6 with hNup153FG depends on the FG-motifs in hNup153FG. a, Schematic overview of the BioID2-DNAJB6b fusion protein and how samples were obtained. Fluorescent image shows HEK293T cells expressing BioID2-DNAJB6b, treated for 24 h with 50 µM biotin and stained with Alexa Fluor 488-conjugated streptavidin, biotinylated substrates are visualized in foci at the NE. **b**, Streptavidin blot belonging Fig. 4a where HEK293T cells expressing V5-DNAJB6b or BioID2-DNAJB6b are treated for 24 h with 50 µM biotin. **c**, Proximity ligation assay (PLA) performed with antibodies against FG-Nups (mAb414) or DNAJB6 alone, or only both secondary antibodies as negative technical controls for PLA. **d**, SDS-PAGE showing increase in HSPA6 levels after heat shock (43 °C for 30 minutes) but not in DNAJB6 KO nor after overexpression of hNup153FG. **e**, GFP-Nup153 full length localizes predominantly to the NE in HEK293T cells. Due to overexpression, there is also small clustering at the NE, but no aggregates can be observed. **f**, GFP-Nup153AG overexpression in HEK293T cells is homogeneously distributed in the cytoplasm. **g**, HEK293T cells overexpressing GFP-Nup153FG and mCherry-DNAJB6b show colocalization in spherical accumulations (arrowheads). **h**, Filter-trap assay of HEK293T cells with GFP-Nup153AG or GFP-Nup153FG overexpression. Three serial 5-fold dilutions were loaded onto cellulose-acetate membranes and probed with anti-GFP antibodies to detect aggregation of the GFP-Nup153FG or GFP-Nup153AG fragment without or with co-overexpression of V5-DNAJB6b. **i**, HEK293T cells overexpressing V5-DNAJB6b or BioID2-DNAJB6b, either with GFP-Nup153FG or GFP-Nup153AG, are treated for 24 h with 50 µM biotin. Biotinylated close proximity partners of DNAJB6b are pulled down by biotin affinity immunoprecipitation with streptavidin beads, run on SDS-PAGE. GFP and DNAJB6 are detected with specific antibodies. Scale bars on all fluorescent images represent 10 µm. Source numerical data and unprocessed blots are available in source data.

https://doi.org/10.1038/s41556-022-01010-x

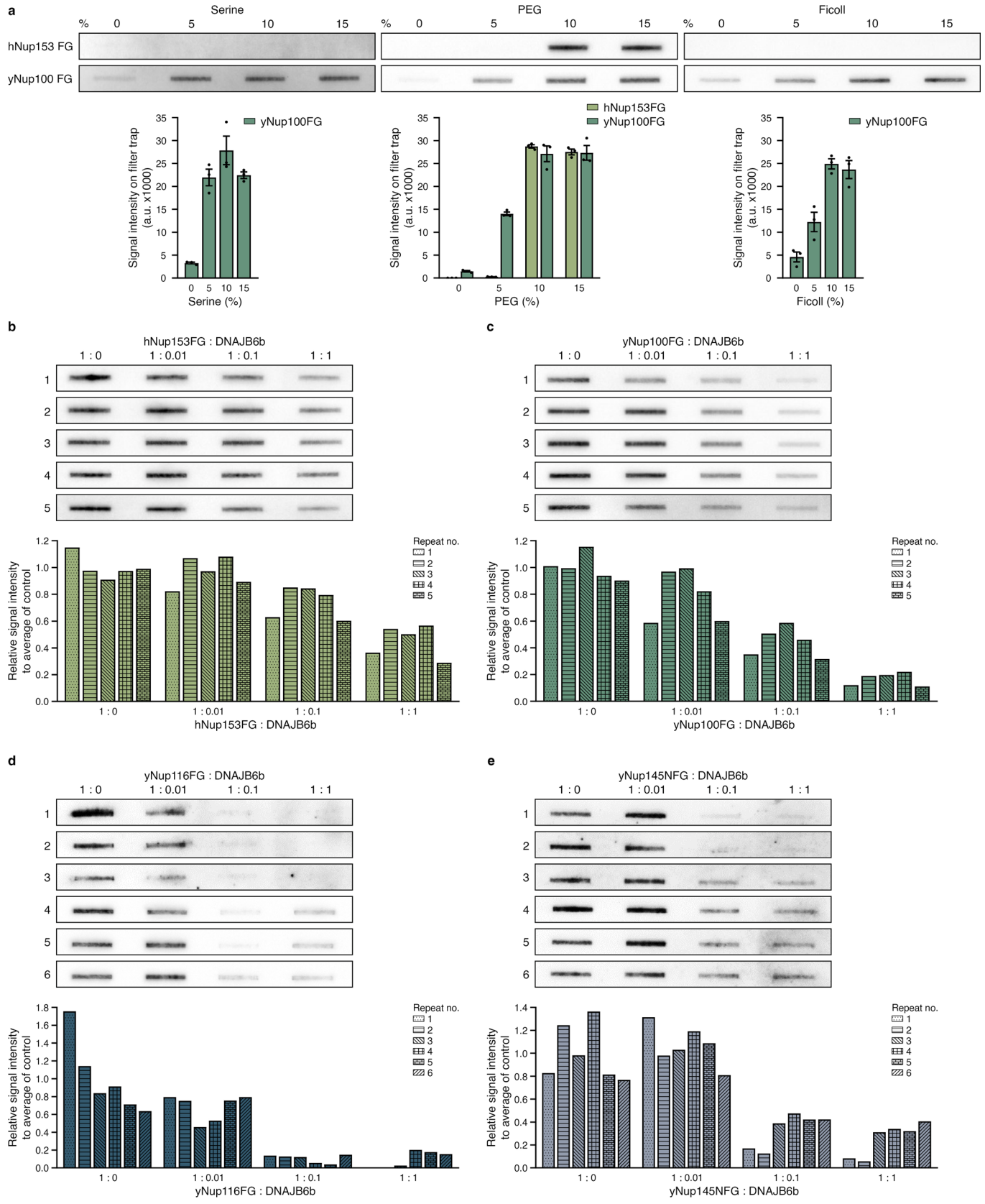

Extended Data Fig. 6 | See next page for caption.

https://doi.org/10.1038/s41556-022-01010-x

Extended Data Fig. 6 | The effect of crowding agents and DNAJB6b on the aggregation of human and yeast FG-Nup fragments in vitro. a, 6 µM of purified FG-Nup fragments were incubated in assay buffer (150 mM NaCl, 50 mM TrisHCl, pH 8) containing the indicated concentration (w/v) of the crowding agents Serine, PEG3350, or Ficoll, at 25 °C for 1 hour, and loaded on a filter trap. Graphs show quantification of Nup band intensity in the described conditions. n = 3 independent experiments; mean ± SEM. hNup153FG did not form any quantifiable bands on filter trap with the addition of Serine or Ficoll. **b-e**, Individual repetitions of the data in Fig. 5a. The effect of DNAJB6b on the aggregation of human and yeast FG-Nup fragments in vitro. Filter trap assays to detect aggregation of purified FG-Nup fragments, incubated with the indicated molar ratios of DNAJB6b, probed with anti-His antibodies to detect FG-Nup fragments. hNup153FG (**b**), yNup100FG (**c**), and yNup116FG (**d**) were incubated in the assay buffer (150 mM NaCl, 50 mM TrisHCl, pH 8) containing 10% PEG3350 (w/v), at 25 °C for either 1 hour (hNup153FG, yNup100FG) or 3 hours (yNup116FG), and yeast Nup145NFG (**e**) was incubated in a buffer comprising 50 mM NaCl, 100 mM sodium phosphate, pH6, 10% PEG3350 (w/v), at 25 °C during 1 hour. Graphs show band intensities on filter trap quantified relative to the average intensity in the absence of DNAJB6b. Source numerical data and unprocessed blots are available in source data.

https://doi.org/10.1038/s41556-022-01010-x

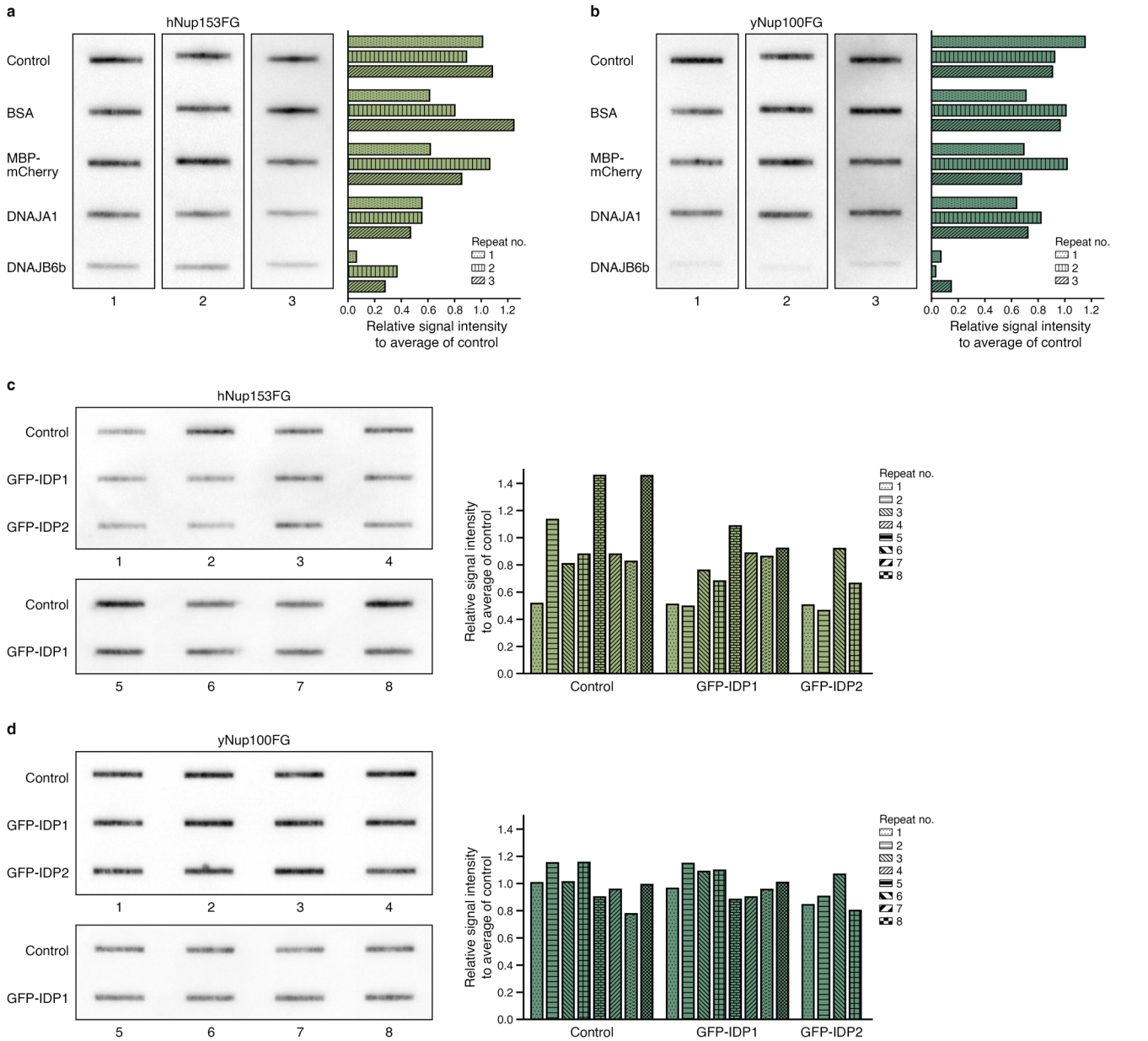

Extended Data Fig. 7 | Individual repetitions of the data in Fig. 5b. a, **b**, The effect of control proteins relative to DNAJB6b on the aggregation of human and yeast FG-Nup fragments in vitro. 6 µM of purified hNup153FG (**a**) or yNup100FG (**b**) were incubated in the absence (control) or presence of BSA, MBP-mCherry, DNAJA1, or DNAJB6b at a 6 µM concentration (molar ratio 1:1). BSA and MBP-mCherry served as non-chaperone controls and DNAJA1 served as chaperone control. Graphs represent band intensities relative to the average intensity of the FG-Nup fragments alone (control) of each replicate. n = 3 independent experiments. **c**, **d**, 6 µM of purified hNup153FG (**c**) or yNup100FG (**d**) were incubated in the absence (control) or presence of the GFP-tagged intrinsically disordered proteins (IDPs) 1 and 2 (IDP1 is the disordered region of yHeh2; IDP2 is a synthetic IDP; for details see methods) at a 6 µM concentration (molar ratio 1:1). Band intensities are quantified relative to the average intensity of the FG-Nup fragments alone. Source numerical data and unprocessed blots are available in source data.

https://doi.org/10.1038/s41556-022-01010-x

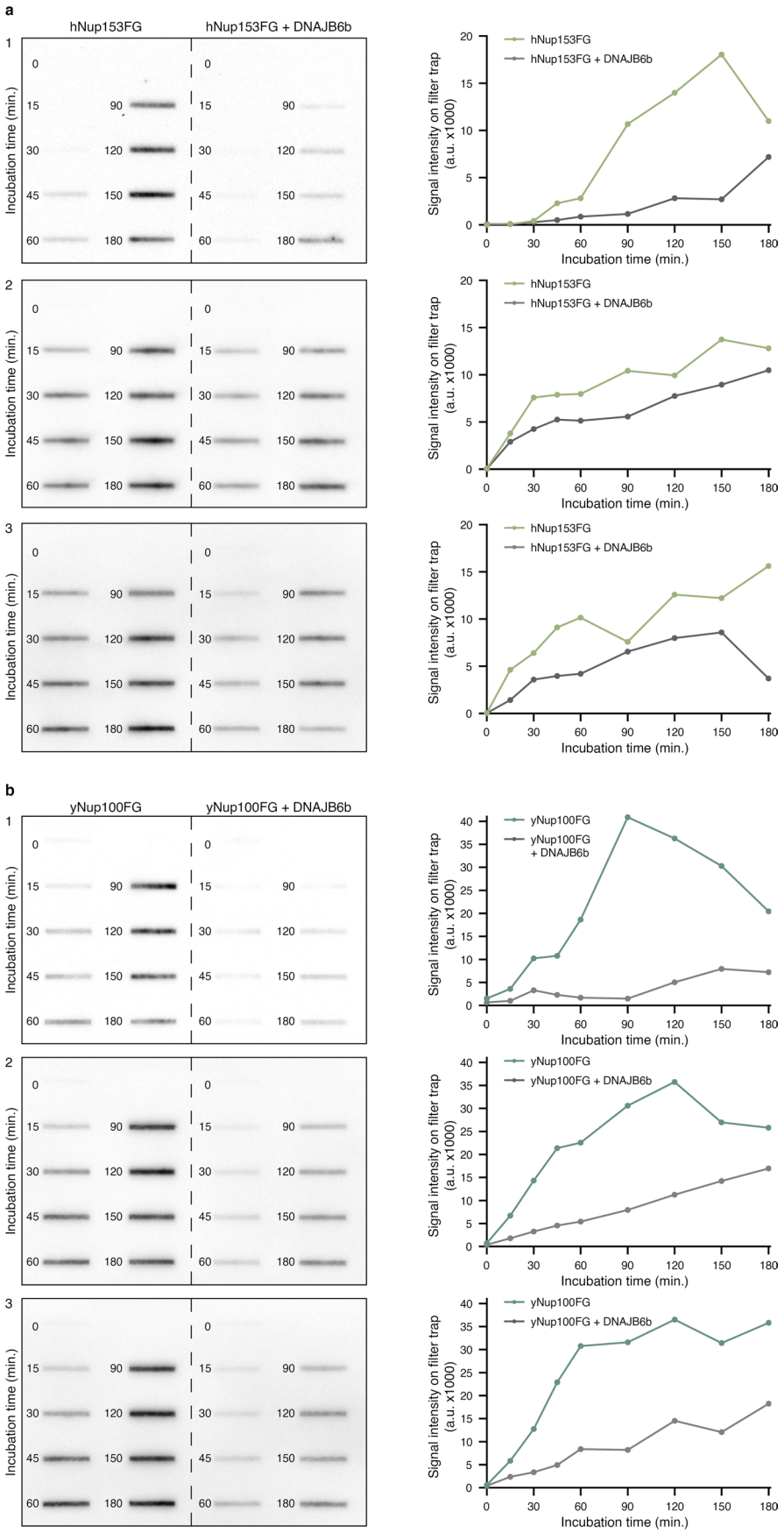

Extended Data Fig. 8 | Individual repetitions of the data in Fig. 5c. a, **b**, The effect of DNAJB6 on the time-dependent formation of hNup153FG and yNup100FG aggregates in vitro. Formation of hNup153FG (**a**) and yNup100FG (**b**) aggregates captured on filter trap over time in the absence and presence of DNAJB6b at a molar ratio of 1:1. Time is indicated in minutes. Graphs depict quantification of Nup band intensity (in arbitrary units, a.u.) over time in the absence (green) or presence (grey) of DNAJB6b. Source numerical data and unprocessed blots are available in source data.

https://doi.org/10.1038/s41556-022-01010-x

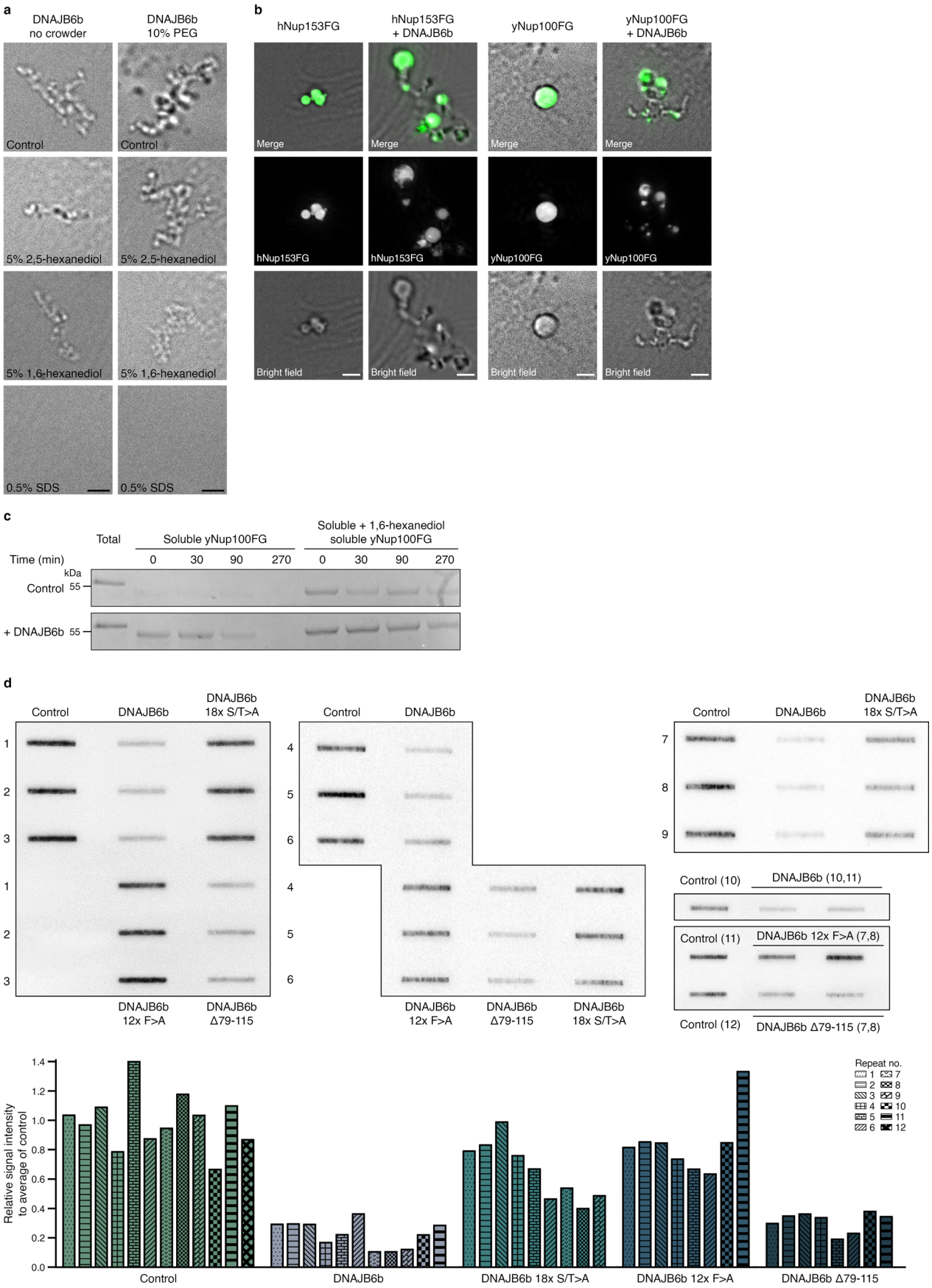

Extended Data Fig. 9 | See next page for caption.

https://doi.org/10.1038/s41556-022-01010-x

Extended Data Fig. 9 | Condensation of DNAJB6b and FG-Nup fragments, and individual repetitions of the data in Fig. 6b. **a**, DNAJB6b condensates by itself and is SDS soluble. Purified DNAJB6b was incubated with or without 10% PEG3350 (w/v). After 1 hour incubation, either 5% 2.5-hexanediol, 5% 1.6-hexanediol, or 0.5% SDS was added for 10 minutes and bright field images were taken. **b**, Fluorescence and bright field microscopy images showing co-localisation of Fluorescein-5-Maleimide labelled hNup153FG and yNup100FG in the absence or the presence of unlabelled DNAJB6b at a 3 µM concentration (molar ratio 1:1). Deconvolved fluorescence images are depicted as maximum Z-Projection of 30 consecutive slices of 0.2 micron. Scale bar represents 2 µm. **c**, Coomassie-stained SDS-PAGE showing one replicate of the sedimentation assay (quantified in Fig. 5e-f) to assess the soluble fraction of yNup100FG (3 µM) in the presence or absence of DNAJB6b (1.5 µM) for the indicated times. To determine the fraction 1,6-hexanediol soluble condensates, 10% 1,6-hexanediol was added for 10 minutes prior to centrifugation. Total yNup100FG protein is slightly shifted on the blot due to effects of PEG on mobility. **d**, Individual repetitions of the data in Fig. 6b. Filter-trap assays showing the effect of wildtype or indicated DNAJB6 mutants (18x S/T > A, 12x F > A, Δ79-115) on the aggregation of yNup100FG (3 µM; molar ratio 1:1). Graphs represent band intensities relative to the average intensity of the yNup100FG fragment alone (control). Source numerical data and unprocessed blots are available in source data.

https://doi.org/10.1038/s41556-022-01010-x

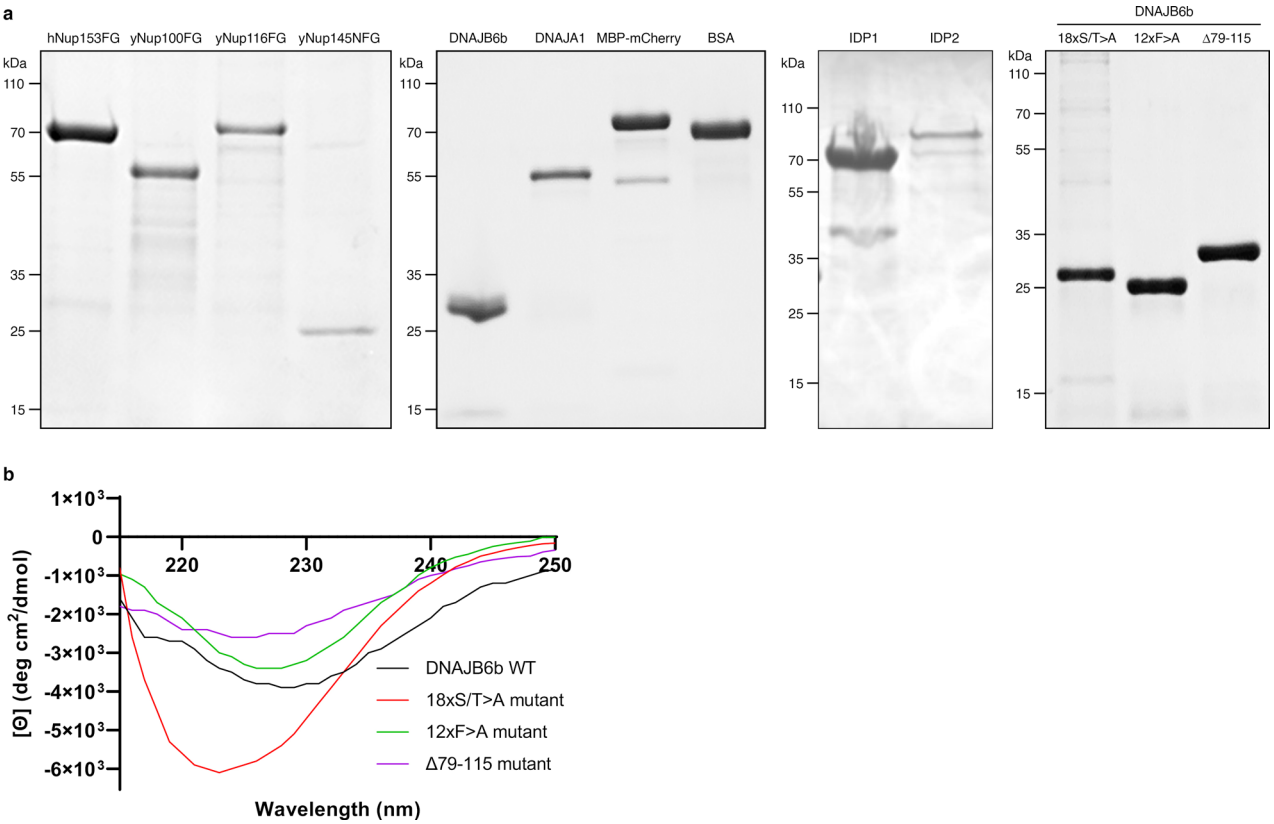

Extended Data Fig. 10 | Characterization of purified FG-Nup fragments, control proteins and DNAJB6 mutants. a, Coomassie Brilliant Blue stained SDS-PAGE of indicated purified protein samples. **b**, Circular dichroism spectroscopy of DNAJB6b and DNAJB6b mutants (18x S/T > A, 12x F > A, and Δ79-115). Purified proteins were diluted to a concentration of either 0.2 µM (DNAJB6b WT), 0.67 µM (18xS/T > A) or 15 µM (12xF > A and Δ79-115) in the assay buffer (50 mM TrisHCl, 150 mM NaCl, pH 8.0). Ellipticity was recorded between 500 and 200 nm in a quartz (QS) cuvette. Data was converted to Molar ellipticity ([q]) to correct for protein concentration, cuvette pathlength and number of backbone peptide units. Source numerical data are available in source data.

nature portfolio

Corresponding author(s): Els Kuiper, Harm Kampinga, Liesbeth Veenhoff, Steven Bergink

Last updated by author(s): Sep 5, 2022

Reporting Summary

Nature Portfolio wishes to improve the reproducibility of the work that we publish. This form provides structure for consistency and transparency in reporting. For further information on Nature Portfolio policies, see our Editorial Policies and the Editorial Policy Checklist.

Statistics

For all statistical analyses, confirm that the following items are present in the figure legend, table legend, main text, or Methods section.

n/a	Confirmed	
☐	☒	The exact sample size (*n*) for each experimental group/condition, given as a discrete number and unit of measurement
☐	☒	A statement on whether measurements were taken from distinct samples or whether the same sample was measured repeatedly
☐	☒	The statistical test(s) used AND whether they are one- or two-sided *Only common tests should be described solely by name; describe more complex techniques in the Methods section.*
☒	☐	A description of all covariates tested
☒	☐	A description of any assumptions or corrections, such as tests of normality and adjustment for multiple comparisons
☐	☒	A full description of the statistical parameters including central tendency (e.g. means) or other basic estimates (e.g. regression coefficient) AND variation (e.g. standard deviation) or associated estimates of uncertainty (e.g. confidence intervals)
☐	☒	For null hypothesis testing, the test statistic (e.g. *F*, *t*, *r*) with confidence intervals, effect sizes, degrees of freedom and *P* value noted *Give P values as exact values whenever suitable.*
☒	☐	For Bayesian analysis, information on the choice of priors and Markov chain Monte Carlo settings
☒	☐	For hierarchical and complex designs, identification of the appropriate level for tests and full reporting of outcomes
☒	☐	Estimates of effect sizes (e.g. Cohen's *d*, Pearson's *r*), indicating how they were calculated

Our web collection on statistics for biologists contains articles on many of the points above.

Software and code

Policy information about availability of computer code

Data collection	LAS-AFX(3.5.7.23225), Flow-Jo (10.5.0) , softWoRx (7.0.0 Release RC6)
Data analysis	IMOD(4.11), ICY (2.4.1.0), Fiji/ImageJ (2.3.0/1.53q), GraphPad prism (9.4.1)

For manuscripts utilizing custom algorithms or software that are central to the research but not yet described in published literature, software must be made available to editors and reviewers. We strongly encourage code deposition in a community repository (e.g. GitHub). See the Nature Portfolio guidelines for submitting code & software for further information.

Data

Policy information about availability of data

All manuscripts must include a data availability statement. This statement should provide the following information, where applicable:

- Accession codes, unique identifiers, or web links for publicly available datasets
- A description of any restrictions on data availability
- For clinical datasets or third party data, please ensure that the statement adheres to our policy

Large scale EM data is available via nanotomy.org http://www.nanotomy.org/OA/Kuiper2022NCB/
Source data have been provided in Source Data. All other data supporting the findings of this study are available from the corresponding author on reasonable request

Field-specific reporting

Please select the one below that is the best fit for your research. If you are not sure, read the appropriate sections before making your selection.

☒ Life sciences ☐ Behavioural & social sciences ☐ Ecological, evolutionary & environmental sciences

For a reference copy of the document with all sections, see nature.com/documents/nr-reporting-summary-flat.pdf

Life sciences study design

All studies must disclose on these points even when the disclosure is negative.

Sample size	No statistical method was used to predetermine sample size. Sample sizes were either above 100 (individual cells) or taken as large as possible; the exact number is indicated in the figure legends
Data exclusions	no data was excluded
Replication	experiments were repeated (n is indicated in the legends), all experiments were reproducible
Randomization	The experiments were not randomized.
Blinding	The investigators were not blinded to allocation during experiments and outcome assessment.

Reporting for specific materials, systems and methods

We require information from authors about some types of materials, experimental systems and methods used in many studies. Here, indicate whether each material, system or method listed is relevant to your study. If you are not sure if a list item applies to your research, read the appropriate section before selecting a response.

Materials & experimental systems

n/a	Involved in the study
☐	☒ Antibodies
☐	☒ Eukaryotic cell lines
☒	☐ Palaeontology and archaeology
☒	☐ Animals and other organisms
☒	☐ Human research participants
☒	☐ Clinical data
☒	☐ Dual use research of concern

Methods

n/a	Involved in the study
☒	☐ ChIP-seq
☐	☒ Flow cytometry
☒	☐ MRI-based neuroimaging

Antibodies

Antibodies used	a list of all antibodies used, name, company, catalogue nr and dilution is provided in the material and method section
Validation	all antibodies were previously used or verified using KO material and tagged constructs. Mouse monoclonal antibodies: RanGap1 (Santa Cruz Biotechnology, sc-28322, 1:500) (Validated with western blot and immunofluorescence) Nup50 (Santa Cruz Biotechnology, sc-398993, 1:250) (Validated with western blot and immunofluorescence) Nup98 (Santa Cruz Biotechnology, sc-74553, 1:500) (Validated with western blot and immunofluorescence) Nup153 (Santa Cruz Biotechnology, sc-101544, 1:150) (Validated with western blot and immunofluorescence) Nup153 (Biolegend, 906201 (QE5), 1:250) (Validated with western blot and immunofluorescence) Nup205 (Santa Cruz Biotechnology, sc-377047, 1:250) (Validated with western blot and immunofluorescence) RanBP2/Nup358 (Santa Cruz Biotechnology, sc-74518, 1:250) (Validated with western blot and immunofluorescence) TPR (Santa Cruz Biotechnology, sc-271565, 1:200) (Validated with western blot and immunofluorescence) mAb414 (Biolegend, 902901, 1:500) (Validated with western blot and immunofluorescence) Lamin B1 (Santa Cruz Biotechnology, sc-365962, 1:500) (Validated with western blot and immunofluorescence) HSP70 (Stressgen, SPA-810, 1:250) (Validated with western blot) HSP70B' (HSPA6) (Enzo Lifesciences, ADI-SPA-754, 1:1000) (Validated with western blot) Ubiquitin (Sigma-Aldrich, ST1200 (FK2), 1:1000) (Validated with western blot) GFP/YFP (Clontech, JL-8, 1:500) (Validated with western blot) His (Qiagen, 34670, 1:1000) (Validated with western blot) GAPDH (Fitzgerald, 10R-G109A, 1:10000) (Validated with western blot) IgGk BP-HRP (Santa Cruz Biotechnology, sc-516102, 1:250) (Validated with western blot) Rabbit polyclonal antibodies:

ELYS (Abcam, ab14431, 1:1000) (Validated with western blot)
DNAJB6 (Braakman lab Utrecht, 1:250) (Kakkar et al, Mol. Cell, 2016 validated on western blot; Thiruvalluvan et al, Mol. Cell 2018 validated with siRNA)

Goat polyclonal antibody:
Nup133 (Santa Cruz Biotechnology, sc-27392, 1:100) (Validated with western blot)

Secondary antibodies:
Anti-Mouse-IgG HRP (GE-Healthcare, GENXA931, 1:5000) (Validated with western blot)
Anti-Rabbit-IgG HRP (GE-Healthcare, GENA934, 1:5000) (Validated with western blot)
Anti-Goat-IgG HRP (Santa Cruz Biotechnology, sc-2020, 1:5000) (Validated with western blot)
Alexa Fluor 488 Donkey anti-Rabbit IgG (H+L) (ThermoFisher, A21202, 1:1500) (Validated with immunofluorescence)
Alexa Fluor 594 Donkey anti-Mouse IgG (H+L) (ThermoFisher, A21203, 1:1500) (Validated with immunofluorescence)
Alexa Fluor 633 Goat anti-Rabbit IgG (H+L) (ThermoFisher, A21070, 1:1500) (Validated with immunofluorescence)
Pierce™ High Sensitivity Streptavidin-HRP (Thermo Scientific, 21130, 1:1500) (Validated with western blot and immunofluorescence)

Eukaryotic cell lines

Policy information about cell lines

Cell line source(s)	U2OS (human osteosarcoma), BeWo (human placenta) HeLa (human cervical cancer), and HEK293T (human embryonal kidney) are standard cell lines. HEK293T cells were obtained from Invitrogen, DNAJB6 KO HEK293T cells were generated using CRISPR-Cas9 knockout strategies. U2OS cells were obtained from the Danish cancer society research center, HeLa and Hela 4TorKO were obtained from Yale school of medicine (gift from C. Schlieker), BeWo cells were obtained from the UMCG pediatrics department
Authentication	HEK293T cells were sequenced, U2OS and HEK293T were recently verified using mass spec. Bewo and HeLa were verified using morphological characteristics
Mycoplasma contamination	all cells are regular checked for mycoplasma, both using PCR and staining (PCR at least twice a year), only mycoplasma negative cells were used for experiments
Commonly misidentified lines (See ICLAC register)	no misidentified cell lines were used

Flow Cytometry

Plots

Confirm that:

☒ The axis labels state the marker and fluorochrome used (e.g. CD4-FITC).

☒ The axis scales are clearly visible. Include numbers along axes only for bottom left plot of group (a 'group' is an analysis of identical markers).

☒ All plots are contour plots with outliers or pseudocolor plots.

☒ A numerical value for number of cells or percentage (with statistics) is provided.

Methodology

Sample preparation	cells were fixed in 70% ethanol overnight at 4°C. DNA content was stained with 50 mg/ml propidium iodide (PI) and 1 mg/ml RNase A for 30 minutes at 37°C in the dark prior to FACS analysis.
Instrument	Beckman Coulter MoFlo Astrios
Software	FlowJo
Cell population abundance	no cell populations were selected, all PI positive cells were analyzed
Gating strategy	no gating was used

☐ Tick this box to confirm that a figure exemplifying the gating strategy is provided in the Supplementary Information.